Hydrodesulfurization of 4,6-Dimethyldibenzothiophene and the Diesel Oil Fraction on NiMo Catalysts Supported over Proton-Exchanged AlMCM-41 and TiMCM-41 Extrudates

Karolina Jaroszewska, Marek Lewandowski, Kinga Góra-Marek, Jolanta Grzechowiak, Gérald Djéga-Mariadassou

catalysts

MDPI

Article

Hydrodesulfurization of 4,6-Dimethyldibenzothiophene and the Diesel Oil Fraction on NiMo Catalysts Supported over Proton-Exchanged AlMCM-41 and TiMCM-41 Extrudates

Karolina Jaroszewska [1,*], Marek Lewandowski [2,3], Kinga Góra-Marek [4], Jolanta Grzechowiak [1] and Gérald Djéga-Mariadassou [5]

1 Faculty of Chemistry, Wrocław University of Science and Technology, 7/9 Gdańska St., PL-50344 Wrocław, Poland; jolanta.grzechowiak@pwr.edu.pl
2 Faculty of Energy and Fuels, AGH University of Science and Technology, 30 Mickiewicza St., PL-30059 Kraków, Poland; lewandowski@agh.edu.pl
3 AGH Centre of Energy, AGH University of Science and Technology, 36 Czarnowiejska St., PL-30054 Kraków, Poland
4 Faculty of Chemistry, Jagiellonian University in Kraków, 2 Gronostajowa St., PL-30387 Kraków, Poland; kinga.gora-marek@uj.edu.pl
5 Laboratoire Réactivité de Surface (LRS), Sorbonne Université, CNRS, 4 Place Jussieu, F-75005 Paris, France; djega.gerald@orange.fr
* Correspondence: karolina.jaroszewska@pwr.edu.pl; Tel.: +48-713206302

Citation: Jaroszewska, K.; Lewandowski, M.; Góra-Marek, K.; Grzechowiak, J.; Djéga-Mariadassou, G. Hydrodesulfurization of 4,6-Dimethyldibenzothiophene and the Diesel Oil Fraction on NiMo Catalysts Supported over Proton-Exchanged AlMCM-41 and TiMCM-41 Extrudates. *Catalysts* **2021**, *11*, 1086. https://doi.org/10.3390/catal11091086

Academic Editor: Jose L. Hueso

Received: 31 July 2021
Accepted: 7 September 2021
Published: 9 September 2021

Abstract: NiMo catalysts supported on mesoporous MCM-41 type materials shaped with binder were tested for activity in the hydrodesulfurization of 4,6-dimethyldibenzothiophene (4,6-DMDBT) and the diesel fuel fraction (0.92 wt% of sulfur). The aim of the investigation was to evaluate the effect of ion exchange with protons of Al- or Ti-substituted MCM-41 mesoporous supports. The subjected catalytic systems were NiMo/HAlMCM-41 and NiMo/HTiMCM-41, and for comparison purposes NiMo/AlMCM-41 and NiMo/TiMCM-41. The samples were characterized by N_2 sorption (at 77 K), XRD, TEM, XPS, SEM and Py–IR. It was found that the functionalization of AlMCM-41 and TiMCM-41 with protons increased the conversion of 4,6-DMDBT and the pseudo-first-order rate constant. Correspondingly, 4,6-DMDBT HDS reactions over the NiMo/HTiMCM-41 catalyst proceeded to a similar extent via hydrogenation and direct desulfurization, whereas over the NiMo/HAlMCM-41 they proceeded mainly via direct desulfurization. Furthermore, the ion-exchanged catalysts displayed two-fold higher efficiency in direct desulfurization than their non-modified counterparts. The NiMo/HTiMCM-41 catalyst exhibited the highest catalytic efficiency in the HDS of 4,6-DMDBT and the diesel oil fraction. The high activity of the NiMo/HTiMCM-41 catalyst is mainly attributed to its appropriate acidity, as well as the metal–support interaction providing both the high dispersion of the active phase and the desirable multilayered stacking morphology of the active phase slabs.

Keywords: hydrodesulfurization; H-AlMCM-41; H-TiMCM-41; ion exchange; acidity; catalyst extruding; binder

1. Introduction

Environmental concerns have imposed stricter regulations on vehicle fuels in order to limit harmful emissions like SO_x and NO_x from exhaust gases. The petroleum industry is currently facing the problem of not only manufacturing clean, high-quality fuels but also producing them from increasingly heavy raw materials. It is well known that a significant part of the reserves of today's extracted crude oil consists of heavy oil fractions with high sulfur, nitrogen, polyaromatic, and metal contents [1]. In order to meet the increasing global motor fuels demand, it has become mandatory to make better use of heavy crude oil fractions like vacuum residues, by hydrocracking them into lighter, useful fractions. At the same time, the still-growing global demand for liquid engine fuels and the depletion

of fossil fuel reserves has led to increasing attention on the liquefaction of alternative raw materials, such as waste tire pyrolysis into high-quality fuels requiring the removal of harmful sulfur compounds [2]. Therefore, over the years, the interest keeps growing for an effective hydrotreating catalyst, mainly for the hydrodesulfurization (HDS) of these heavy fractions. The limit for the clean fuel specifications with respect to the sulfur content is set to lower than 10 ppm level [3–6]. Although today's HDS technology is effective and able to provide this level of desulfurization, it is often considered to be high-priced. The process of the hydrodesulfurization of heavy fractions (where the concentration of sulfur compounds is the highest) is realized in two stages. In the first one, the amount of sulfur is removed to a level of 300–500 ppm; this process is relatively easy [7]. Further desulfurization is more difficult because it concerns the compounds in which the access to sulfur is more difficult for steric reasons (e.g., 4,6-dimethyldibenzothiophene, 4,6-DMDBT). The elimination of sulfur from such molecules requires more drastic conditions of the process, which are related to increasing costs. Thus, the HDS technology is known to be financially tasking in terms of its operational conditions, which require a resistant solid catalyst as well as high temperature (up to 400 °C) and hydrogen gas pressure conditions (up to 100 atm) [6,8].

Therefore, cheaper but efficient HDS technologies are continuously required. It seems that the effective solution would be the discovery of an advanced HDS catalyst showing high activity in hydrodesulfurization reactions. The hydrodesulfurization of 4,6-DMDBT goes via three pathways: hydrogenation (HYD), direct desulfurization (DDS), and the acidic method, mainly isomerization (ISOM) followed by DDS (Figure 1).

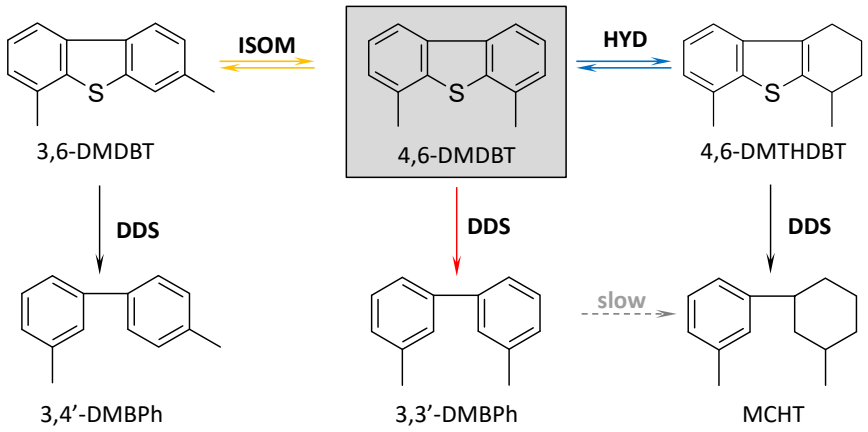

Figure 1. Reaction network of the HDS of 4,6-dimethyldibenzothiophene (4,6-DMDBT), 4,6-dimethyltetrahydrodibenzothiophene (4,6-DMTHDBT), 3-(3′-methylcyclohexyl)-toluene (MCHT), 3,3′-dimethylbiphenyl (3,3′-DMBPh), 3,6-dimethyldibenzothiophene (3,6-DMDBT) and 3,4′-dimethylbiphenyl (3,4′-DMBPh). HYD, hydrogenation; DDS, direct desulfurization; ISOM, isomerization.

The acidic route was observed for catalysts such as zeolites, which presented Brønsted acid sites at their surface. It has been reported that the Brønsted acid sites can facilitate the formation of coordinatively unsaturated sites (CUS) and further prompt the DDS route through the cracking of C–S bond in sulfides for the HDS reaction [9]. The increase of the acidic function of the catalyst improves its performance because it catalyzes the skeletal rearrangement of the alkyl substituent in the 4,6-DMDBT molecule, which reduces the steric hindrance, allowing the easier access of the sulfur to the catalyst's active site [10].

The industrial HDS process employs catalysts composed of Mo or W species promoted by metals with vacant d orbitals such as Ni ($3d^8$) or Co ($3d^7$) deposited on alumina. The active phase of these catalysts is the so-called Co(Ni)-Mo(W)-S species, where the active sites are CUS located at the edges of the $Mo(W)S_2$ slabs. Many studies have shown that the activity and selectivity of the catalysts are correlated not only to the reducibility, size and arrangement of the active phase but also are significantly influenced by the acidic

properties of the carriers, especially Brønsted acidity [11,12]. Moreover, many studies have tried to improve the performance of hydrotreating catalysts by doping the alumina support with acidic agents, such as fluorine, boron, phosphorus, and zeolites [13,14]. The catalytic performance of the conventional HDS catalysts can be modified by replacing the alumina with other materials, leading to an important improvement of the HDS activity. In the past few years, much consideration has been given to the application of mesoporous materials such as MCM-41 as supports for the hydrotreating of catalysts [15–20]. The potential advantages of the use of mesoporous materials are their high surface area, uniform pore size, and the possibility of the modification of their surface properties, i.e., the acidity via framework substitution of Al. The results of HDS studies involving MCM-41 supported catalysts reported in the literature mainly refer to the desulphurization of dibenzothiophene (DBT) over catalysts prepared using AlMCM-41. It has been also found that the incorporation of Ti into MCM-41 and HMS increases the catalytic activity in the DBT HDS reaction [16,19]. It has been revealed that the initial DBT HDS activity of the NiMoW/TiSBA-16 catalyst prepared by the sol-gel method doubled that of a commercial NiMo/γ-Al_2O_3, which was linked with its better textural properties, acidity and adequate active phase dispersion [11]. In a study of Nava et al. [21], it was demonstrated that CoMo/TiSBA-15 showed a higher catalytic activity than their Ti-free counterparts, due to the enhancement of the DDS route in this reaction. The differences observed in the catalyst performance were attributed to the structure and specific electronic properties of the supported active phases, due to a higher Lewis acidity than the Ti-free samples. Cao et al. [9] found that the HDS of the DBT efficiency can be significantly improved by the incorporation of Al and Ti atoms into NiMo/Al-Ti-SBA-16 catalysts through the enhancement of the acidity and properties of the active metals. It has been reported that the Brønsted acid sites can facilitate the formation of S-edge sites, which further facilitate the DDS selectivity. The recent investigation of Huirache-Acuña et al. [16] showed the influence of Ti substitution in ternary sulfided NiMoW/Ti-HMS mesoporous catalysts on the DBT HDS performance. Ti-incorporation improved the catalytic efficiency by up to 2.4 times relative to the non-Ti-modified catalyst and to an industrial catalyst. The authors ascribed the high activity of Ti-doped catalysts to the differences observed in the stacking, length and dispersion of the active phase, which strongly enhanced the catalytic activity and sulfur removal via the HYD route. The ion-exchange of mesoporous materials is an effective way to improve the surface acidity due to the protons' immobilization. Nevertheless, the influence of the functionalization with surface protons of the MCM-41 sieves has been studied only in the case of proton-exchanged siliceous [22,23] or alumina siliceous materials [24] in HDS reactions, but never the titanium ones. However, protonated titanium materials, such as titanate nanotubes, have been shown to be active materials in acidic catalysis [25,26]. The literature data show that great progress has been made in the synthesis of catalysts for the HDS process; however, the design of the catalyst's composition still remains a challenge to achieve the optimum activity, feasibility and economic profitability. It seems that combining the advantages of the incorporation of Al and Ti species into MCM-41 support and ion exchange should be an effective way to improve the HDS efficiency.

The aim of this study is to ascertain how the modification of the MCM-41 sieves with Al or Ti substitution and proton incorporation affects the features and activity of NiMo catalytic systems. To the best of the authors' knowledge, no paper considering that effect in the case of MCM-41 supports has been published so far. In addition, most of the works refer to the supports in powder form. This investigation concerns the characterization and catalytic activity of NiMo catalyst-supported MCM-41 materials extruded with a binder (here γ-Al_2O_3). This allows us to follow the properties of the catalysts, which are similar to the commercial catalysts, i.e., they are shaped with a binder. Studies on mesoporous materials do not take into account that aspect. Thus, it would be of interest to compare the activity of NiMo/HAlMCM-41 and NiMo/HTiMCM-41 in the HDS of the most refractory sulfur compounds, such as 4,6-DMDBT and the diesel fuel fraction originating from fluid catalytic cracking with a 0.92 wt% sulfur concentration.

2. Results and Discussion

2.1. Characterization of Supports and Catalysts

The low-temperature N_2 adsorption–desorption isotherms are plotted in Figure 2, and the texture parameters are itemized in Table 1. According to the IUPAC classification, the HTiMCM-41 and HAlMCM-41 materials present isotherms of type IV (Figure 2A,B), showing a sharp inflection at a relative pressure of around p/p_0 = 0.3–0.4, which is characteristic of well-ordered mesoporous sieves [27]. However, the second inflexion and hysteresis of type H3 can be observed for the samples above the relative pressure of 0.45, which is attributed to the capillary condensation of nitrogen within the interparticles, macropores, and/or some impurity phases (e.g., aluminium or titanium species which have not been substituted in the structure of the material). Evidence for the presence of a highly ordered hexagonal structure in the HAlMCM-41 and HTiMCM-41 samples is provided by TEM micrographs and XRD patterns, as shown in Figure 2 (as an insertion). It should be noted that the extrusion with a binder followed by impregnation resulted in a decrease of the nitrogen uptake step, indicating the limitation of the mesopore volume in NiMo/HAlMCM-41 and NiMo/HTiMCM-41 catalysts. Isotherms of both catalysts should be ascribed to IV curves; however, the step gradually becomes flat upon shaping with a binder followed by Ni and Mo oxides. Moreover, the incorporation of the NiMo phase and shaping with a binder significantly decreased the textural parameters of the catalysts, pointing to the location of significant NiMo sites inside the mesopores (Table 1). The XRD pattern of the NiMo/HTiMCM-41 sample (Figure 2B) confirms a well-ordered structure, but the diffractogram of the NiMo/HAlMCM-41 (Figure 2A) catalyst is not so conclusive as for the parent material. It suggests that the framework structure is partly disordered under the influence of the catalyst preparation procedure.

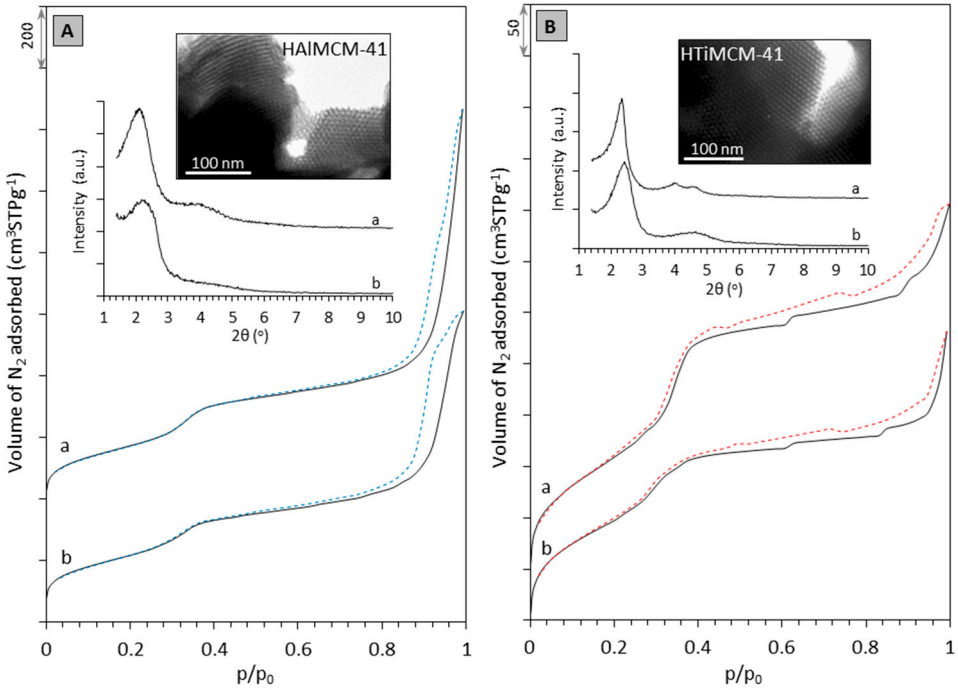

Figure 2. Characterization (N_2 isotherms, XRD patterns and TEM images) of (**A**) Al-containing samples: (a) HAlMCM-41 and (b) NiMo/HAlMCM-41; and (**B**) Ti-containing samples: (a) HTiMCM-41 and (b) NiMo/HTiMCM-41.

The results revealed that the incorporation of Ti and Al into MCM-41, its extrusion with a binder, and incipient wetness impregnation cause the partial deterioration of the mesoporous structure, which is more significant in the case of the HAlMCM-41-containing sample.

Table 1. Textural properties of the calcined MCM-41 materials, shaped with binder supports and the catalysts.

Sample	S_{BET} ($m^2\ g^{-1}$)	V_T [a] ($cm^3\ g^{-1}$)	d_{BJH} [b] (nm)
H-AlMCM-41	534.3	0.36	2.8
NiMo/HAlMCM-41	329.1	0.44	2.8
H-TiMCM-41	745.9	0.48	2.8
NiMo/HTiMCM-41	483.4	0.58	2.6

[a] Total pore volume determined at $p/p_0 > 0.99$; [b] Pore diameter (BJH method).

2.2. Acidity by Py–IR

The Py–IR spectra with the adsorbed pyridine for all of the samples examined are shown in Figure 3. These spectra show the presence of protonated pyridine ions (PyH^+) on the Brønsted acid sites (at about 1545 and 1640 cm^{-1}), and coordinated pyridine adducts (PyL) on the Lewis acid sites (at about 1620 and 1450–1445 cm^{-1}) [28]. The peak at 1490 cm^{-1} is assigned to the pyridine adsorbed on both the Brønsted and Lewis acid sites [29]. The bands at 1440 cm^{-1} clearly observed in the H-TiMCM-41 series could correspond to Py interacting with Lewis sites of low strength, or alternatively could originate from physically adsorbed pyridine [30].

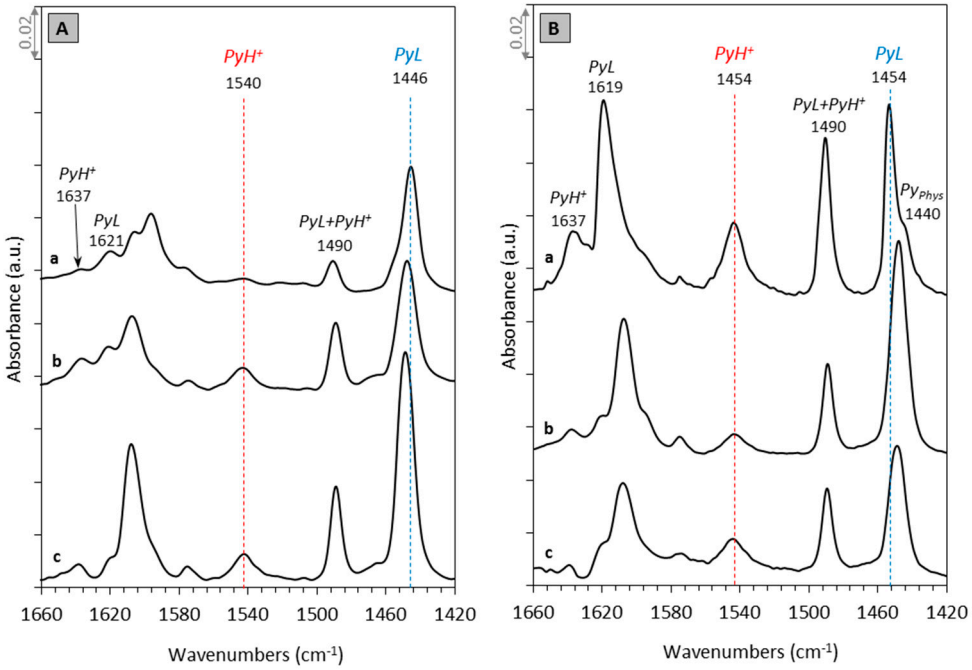

Figure 3. FTIR spectra of pyridine adsorbed at 130 °C on (**A**) AlMCM-41-containing samples: (a) H-AlMCM-41, (b) NiMo/AlMCM-41, and (c) NiMo/H-AlMCM-41; as well as (**B**) TiMCM-41-containing samples: (a) H-TiMCM-41, (b) NiMo/TiMCM-41, and (c) NiMo/H-TiMCM-41.

Table 2 lists the concentration of the acid sites of each catalyst quantitatively calculated from the Py–IR spectra obtained after pyridine desorption at 130 °C. In general, in comparison with the nominal Al and Ti concentrations, all of the samples were characterized by a low number of Brønsted and Lewis acid sites due to the smaller share of Al and Ti atoms exposed on the external surface in comparison to those hidden in the mesopore walls. In fact, the Brønsted acidity value for the H-AlMCM-41 sample is similar to those reported elsewhere for HAlMCM-41 materials [31]. Moreover, protonated HAlMCM-41 shows a lower amount of both Lewis and Brønsted acid sites compared to those of HTiMCM-41, and it is in agreement with the work of Araújo et al. [32]. Therefore, it can be concluded that the Ti atoms are located more favorably than the Al atoms on the surface of the

mesopore walls, giving rise to their higher accessibility to Py and reagent molecules. The dispersion of the active phase (NiO and MoO_3) and its reduction can also be positively influenced by more exposed Ti atoms. In the case of the HAlMCM-41 sample, the Lewis acid sites can originate from extra-framework Al species (EFAL) present in the form of Al^{3+}, AlO^{+}, $Al(OH)_2{}^{+}$, $Al(OH)^{2+}$ or charged $Al_xO_y{}^{n+}$ clusters within the sample, where they are represented as $Al_aO_bH_c{}^{n+}$ [33]. The Brønsted acid sites are the bridging hydroxyl Si-(OH)-Al groups between the tetrahedral aluminum and silicon atoms (FAL) [32]. Such Si-(OH)-Al sites are, however, characterized by a lower strength than that of bridging hydroxyls in zeolitic materials [34]. The formation of Lewis acid sites is also more pronounced in mesoporous aluminosilicates (or titanosilicates), because the extraction of Al (or Ti) atoms from the mesoporous matrix is easier than that from their crystalline counterparts, i.e., zeolites. Furthermore, the presence of some residual ions affects the acidity of the Al- and Ti-substituted and protonated MCM-41 samples. With the HAlMCM-41 sample, there is a possible interaction of the surface residue sulfuric ions (which come from the Al precursor, i.e., $Al_2(SO_4)_3 \times 18\ H_2O$) with Si–OH and Al–OH, leading also to the formation of extra-framework Al species [33]. In the case of the HTiMCM-41 sample, the Lewis acidity is generated by coordinatively unsaturated and saturated titanium ions, possibly derived from titanium with four (monopodal and tripodal modes), five, or six coordination numbers (extra-framework TiO_2 or the hydration of Ti^{4+} ions) [32,35]. The Brønsted acidity in TiMCM-41 is created by the formation of acidic titanols and silanols [12]. Whereas the protonation effect of TiMCM-41 on the acidity was not explored in the literature, other Ti-containing materials, such as titanate nanotubes, were widely investigated in this regard. The results indicate that ion-exchanged sites in the interlayer spaces of the titanate nanotubes do not display a function of Brønsted acid sites, but those on the surface of the titanate nanotubes play the role of proton donors [36]. The inducing of Brønsted acidity in the protonated titanate nanotubes is explained by some of the structural factors [37]. In line with the works of [36,38–40], the acid sites in the H^+-exchanged titanate nanotube were generated by the hydroxyl groups on the scrolled titanate nanosheets. Although the acid strength of H^+-exchanged titanate is weak, the hydroxyl groups pointing towards the center of the nanotube may lead to a strong electric field that behaves as a strong acid site. The distortion in the rolled-up sheets of protonated titanate may also increase the acidity of the hydroxyl groups due to its high strain energy [41]. Taking into account the shape of TiMCM-41 mesopores, i.e., cylindrical tubes, it can be assumed that the same geometrical factor plays a role in creating the Brønsted acidity in protonated HTiMCM-41, but this requires further detailed research. In line with the A_{260}/A_0 values (Table 2), the strength of the Lewis acid sites also changes upon shaping with a binder and the deposition of the active phase (NiO and MoO_3); however, while in HAlMCM-41 the increase of the strength of the Lewis sites is observed, in the HTiMCM-41 series the average strength declines.

Table 2. Acidity of the MCM-41 materials and MCM-41-supported NiMo catalysts by Py–IR.

Sample	*PyH*$^+$ [a]		*PyL* [b]		*PyH*$^+$ + *PyL* [c]
	($\mu mol_{Py} g_{cat}^{-1}$)	A_{260}/A_0 [d]	($\mu mol_{Py} g_{cat}^{-1}$)	A_{260}/A_0 [d]	($\mu mol_{Py} g_{cat}^{-1}$)
H-AlMCM-41	18	0.23	150	0.42	168
NiMo/HAlMCM-41	41	0.19	250	0.42	291
NiMo/AlMCM-41	37	0.47	140	0.74	177
H-TiMCM-41	220	0.39	250	0.60	470
NiMo/HTiMCM-41	100	0.40	200	0.48	300
NiMo/TiMCM-41	32	0.50	245	0.54	277

[a] Brønsted acid sites; [b] Lewis acid sites; [c] total acidity. [d] The strength of the Brønsted and Lewis sites was determined in thermodesorption studies, and was calculated as A_{260}/A_0 ratio, where A_0 denotes the absorbance after the chemisorption of Py at 130 °C, and A_{260} after the desorption of Py at 260 °C.

The acidity measurements have also revealed that shaping with a binder and the deposition of the active phase (NiO and MoO_3) on HAlMCM-41 and HTiMCM-41 sup-

ports has a substantial influence on the final acidity of the catalysts. The preparation of NiMo/HAlMCM-41 leads to a significant increase in the total acidity. The concentration of Brønsted centers increases approximately two-fold in comparison to the neat HAlMCM-41 sample, whereas the concentration of the Lewis centers for the NiMo/HAlMCM-41 material increases by about 65%. In the case of the HTiMCM-41-containing sample, the opposite phenomenon is observed, and the acidity diminution is noticed over the NiMo/HTiMCM-41 catalyst relative to the HTiMCM-41 support. The NiMo/HTiMCM-41 catalyst preparation may bring an approximately two-fold decrease in the quantity of Brønsted acid sites, while the amount of Lewis sites dropped less significantly, as compared with HTiMCM-41. The increase in the Lewis acid site concentration (NiMo/HAlMCM-41) or the preservation of this electron-acceptor function (NiMo/AlMCM-41, NiMo/HTiMCM-41, and NiMo/TiMCM-41), besides undoubtedly covering the mesopore surface with the metal phase (Table 1), can be ascribed to the presence of highly exposed unsaturated Ni and Mo cations. Still, the accessibility of the electron-acceptor species is ruled by the different acidic properties of the HAlMCM-41 and HTiMCM-41 supports [42].

It was also found here that the impregnation of oxides onto the HTiMCM-41 and the shaping procedure reduces the strength of electron-accepting centers and proton centers. Despite the contrary trend in the behavior of the impregnated materials, it is observed that NiMo/HTiMCM-41 displays a slightly higher value of the total acidity, with a higher strength relative to NiMo/HAlMCM-41. The Py thermodesorption data followed the trend of the altered position of the PyL band, originally located at 1446 cm^{-1} and 1454 cm^{-1} in HAlMCM-41 and HTiMCM-41, respectively. The subsequent modifications lead to the enhancement of the strength of Lewis sites for HAlMCM-41, as manifested by the upshift of the PyL band to 1448 cm^{-1}, whereas the drop of strength was observed in the HTiMCM-41 series; the PyL band shifts to lower frequencies (1450 cm^{-1}). This dropping of the number of the Lewis sites accessible for Py and originating from Ti species (represented by the 1454 cm^{-1} PyL band) can be indicative of the preferential location of the NiO and MoO_3 phases on Ti sites.

In order to explain the differences in the acidity of NiMo/HAlMCM-41 and NiMo/HTiMCM-41, one may consider many factors influencing their final surface properties. In general, the deposition of metal oxide clusters into the acidic supports induces two opposite effects. Firstly, the introduced metal cationic species could cover some of the acidic sites originating from the support, bringing the decrease of both types of acid sites. Secondly, the new Lewis and Brønsted acid sites may also be created as a result of interactions between the metal precursor and the support during the impregnation procedure, i.e., due to the metal−support interactions (MSI). An important aspect that should be also addressed in the acidity discussion concerns the effect of the introduction of an additional catalyst component, i.e., a binder.

It is evident that the incorporation of the oxide phases of Ni, Mo and the binder into the HAlMCM-41 material generates a significant increase in the number of acid sites. The electron-deficient species from active-phase components may serve as a kind of newly created Lewis acid site, which recompenses the primary Lewis acidity originating from the parent HAlMCM-41 and being overlapped during impregnation [43,44]. The relatively high Lewis acid site concentrations in the NiMo/HAlMCM-41 can be also ascribed to the presence of the alumina binder (γ-Al_2O_3). As noticed, the NiMo/HAlMCM-41 contains more Brønsted acid sites than the initial HAlMCM-41. This created acidity is attributed to newly formed acid sites as a result of the chemical reactions between HAlMCM-41 and the binder. It is possible that the incorporation of the alumina binder not only accounts for the increase in the Lewis acidity but also contributes to the formation of Brønsted sites. Through the calcination of the drawpieces, pseudoboehmite (all Al in a six-fold coordination) is converted to γ-Al_2O_3 (Al in six-, four- and five-fold coordination), releasing water that in turn promotes the mobility of aluminum species [45].

Over the NiMo/HTiMCM-41 catalyst, a drop of acidity should be attributed to an increasing role of the covering phenomenon of some of the existing acid centers by active-

phase precursors and the binder. Indeed, the enrichment of the MCM-4 surface with Ti atoms (Table 1) was postulated to facilitate the dispersion of the oxide phase. It cannot, however, be excluded that some interaction between Ni and Mo accounts for the formation of some new acid sites. It has also been corroborated that MoO_x additives generate Brønsted acidity on titania surfaces [46,47].

Furthermore, it is worth noting the differences in both the number and strength of Brøntsed and Lewis sites between ion-exchanged catalysts, and that these were not functionalized with protons. It was found that ion exchange leads to only a slight increase in the Brønsted acid sites' number in Al-containing samples (compare NiMo/HAlMCM-41 and NiMo/AlMCM-41). Meanwhile, in the case of Ti-modified samples, unexpectedly, the improvement is much more pronounced (compare NiMo/HTiMCM-41 and NiMo/TiMCM-41). Nevertheless, these findings are in agreement with those observed for neat HAlMCM-41 and HTiMCM-41 materials, showing a significant Brønsted acidity in HTiMCM-41. The results revealed also that an ion exchange decreases the strength of the acid sites of both types (A_{260}/A_0).

To sum up, it is essential to highlight the significance of the nature of the support for the acidity given that, although the catalysts comprise the same active phases (NiMo) and binder, their acidity is considerably different. It was found that through the ion exchange of the Ti-modified MCM-41 support, an NiMo/HTiMCM-41 catalyst with acidic characteristics superior to those of NiMo/HAlMCM-41 is achieved.

2.3. XPS

An appropriate way to monitor the interaction of NiMo species with the support surface consists in studying the materials by XPS. Two representative XPS spectra recorded on the NiMo/HAlMCM-41 and NiMo/HTiMCM-41-reduced samples (at 450 °C) are shown in Figure 4. The binding energy (BE) data obtained after the deconvolution of the main peak for molybdenum-containing species are presented in Table 3.

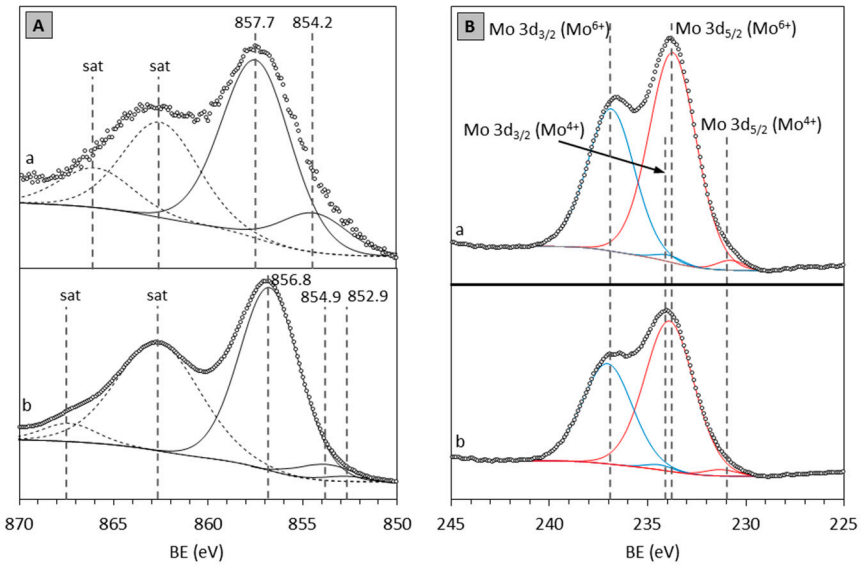

Figure 4. The XPS spectra of (**A**) the Ni $2p_{3/2}$ region, and (**B**) the Mo $3d_{5/2}$ and Mo $3d_{3/2}$ regions for the reduced (**a**) NiMo/HAlMCM-41 and (**b**) NiMo/HTiMCM-41 samples.

As illustrated in Figure 4(Aa), the XPS spectrum of the NiMo/HAlMCM-41-reduced sample presents signals centered on BE values of 854.4 eV and 857.7 eV, which are assigned to the spin-orbit splitting of Ni $2p_{3/2}$ of Ni^{2+} species. The first band can be attributed to Ni species with weak MSI, whereas the second one can be assigned to Ni species with stronger interactions with the support [48]. The Ni oxide species that may be present on the surface of the NiMo catalysts supported over alumina and silica-alumina carriers (i.e.,

the most-used supports for NiMo catalysts), as a consequence of the calcination process, correspond to NiO, Ni_2O_3, $Ni(OH)_2$, $NiMoO_4$ (a product of the reaction of Ni with MoO_3), $NiAl_2O_4$ spinel (a product of the reaction of Ni with Al_2O_3) and $NiSiO_3$ (a product of the reaction of Ni with SiO_2).

Table 3. Mo 3d binding energies of calcined and reduced bimetallic catalysts.

Catalyst	Mo $3d_{3/2}$ (eV)		Mo $3d_{5/2}$ (eV)	
	Mo^{4+}	Mo^{6+}	Mo^{4+}	Mo^{6+}
NiMo/HAlMCM-41	232.9	235.5	229.8	232.6
NiMo/HAlMCM-41 *	233.7	237.1	230.8	234.1
NiMo/HTiMCM-41	233.4	236.2	230.2	233.1
NiMo/HTiMCM-41 *	234.7	237.3	231.5	234.1

* Samples after reduction at 450 °C for 30 min.

As such, the signal at ca. 854.4 eV is attributed to Ni^{2+} in an octahedral coordination of NiO_{bulk} [49]. That type of NiO_{bulk} with no interaction (or a weak interaction) with the support is termed a 'free state NiO'. The presence of stoichiometric NiO at a BE of ca. 854.4 eV, which is slightly lower than the 855.0 eV characteristic for pure NiO, suggests a weak interaction with the support in NiMo/HAlMCM-41. The peak at around 857.7 eV corresponds to the Ni species interacting with the support. In line with the observations of Fang et al. [50], that band can be linked to very small crystallites of NiO located on the framework wall of the MCM-41 mesostructure, i.e., $NiO_{surface}$ (in his work, the Ni/AlMCM-41 catalyst was investigated, and the peak was observed around 357.2 eV). This signal also nearly corresponds to the BE value reported for $NiSiO_3$ species (ca. 857.5 eV) in a Ni/SiO_2 catalyst [51]. The BE at ca. 857.7 eV can be also associated with the presence of Ni_2O_3 over the NiMo/HAlMCM-41 surface [52]. In addition, based on references [53–55], the signal at a higher BE (ca. 857 eV) can be assigned to $NiMoO_4$ or $NiAl_2O_4$ species. All of the values of BE for the Ni species mentioned above are close to each other, and this suggests that these nickel species, i.e., Ni^{2+} and Ni^{3+}, may coexist on the surface of the NiMo catalyst. Nevertheless, the presence of only small peaks below 857.7 eV along with the position of the strong shake-up satellite peaks, centered approximately at 862.8 and 866.3 eV, prove that a small amount of the NiO phase is present on the surface of the catalyst, and the Ni^{2+} species may consist of $NiAl_2O_4$, $NiSiO_3$ and $NiMoO_4$ [56,57].

As can be observed in Figure 4(Ab), in the Ni $2p_{3/2}$ XPS spectrum of the reduced NiMo/HTiMCM-41 catalyst, a subpeak is positioned at around 854.9 eV, and the main signal is at about 856.8 eV. Therefore, a significant shift in BE is observed for NiMo/HTiMCM-41 compared to the NiMo/HAlMCM-41 sample. For the reduced NiMo/HTiMCM-41 catalyst, apart from the discussed peaks, the small peak at 852.9 eV corresponding to the Ni^0 species appears [58]. These results are in good agreement with earlier reports on the better susceptibility to the reduction of Ni species deposited over Ti-modified materials relative to Al-modified ones [59].

The XPS patterns of Mo3d in the range of 225–245 eV are displayed in Figure 4B. The XPS spectrum of the reduced NiMo/HAlMCM-41 catalyst (Figure 4(Ba)) is characterized by two well-resolved contributions at BEs of 233.7 and 237.1 eV, which can be assigned to the Mo $3d_{5/2}$ and Mo $3d_{3/2}$ spin-orbit components of Mo (VI), respectively [60]. Meanwhile, the spectrum of the reduced NiMo/HTiMCM-41 sample in the Mo 3d region shows the presence of spectral lines at 234.7 and 237.3 eV (Figure 4(Bb)). In both cases, the values of BE are somewhat higher than those usually observed at for stoichiometric MoO_3 (232.9 and 236.1 eV) [61], suggesting some interactions of molybdenum species with the support surface. The less-intense signals for the Mo $3d_{5/2}$−Mo $3d_{3/2}$ doublet (i.e., BE at 230.8 and 234.1 eV, and at 231.5 and 234.1 eV for the NiMo/HAlMCM-41 and NiMo/HTiMCM-41 samples, respectively) are linked with the presence of Mo (IV) [62].

Let us to compare the position of the peaks in the XPS spectra for the catalysts tested (Table 3). One may note that, for the HTiMCM-41 based samples, the BE are shifted to

higher values compared to those based on HAlMCM-41 counterparts. It is commonly accepted that the strength of the interaction between molybdenum species and the support is reflected by the BE value, i.e., a stronger Mo−support interaction provides a higher BE. It could be concluded that the Mo−support interaction over HTiMCM-41 is stronger than that over HAlMCM-41. This result points to an increase in the strength of MSI in the NiMo/HTiMCM-41 sample compared to the NiMo/HAlMCM-41. The observations reported here are consistent with those published by Méndez et al. [63]. They demonstrated stronger metal–support interactions in NiMo/TiMCM-41 catalysts than in NiMo/AlMCM-41. Nevertheless, the absolute value of the chemical shift in BE varies in a number of articles because of differences in the molybdenum concentration, type of support, Mo loading procedure, Mo precursor, and spectra calibration. The changing values of the BE of the Mo(VI) ions might also reflect the presence of molybdenum particles of different sizes and forms, and the shifts toward higher BE are indications of the increasing dispersion of Mo species [64].

The strong MSI interactions affect the final properties of the NiMo catalyst in two opposite ways. On the one hand, the strong MSI may result from the formation of inactive species such as $NiAl_2O_4$ or $Al_2(MoO_4)_3$ [65]. Therefore, it could be expected that the replacement of Al atoms with Ti atoms in the MCM-41 framework can efficiently prevent the formation of strong Mo–O–Al and Ni–O–Al linkages. On the other hand, such strong MSI may provide a better dispersion of the active phase, ensuring its homogeneous distribution [66]. Molybdenum was observed to disperse on the titania support in a stable configuration that resists segregation and sintering [67,68]. These results are in agreement with observations on SEM micrographs (Figure 5) which revealed the homogenous dispersion of the Mo phase over a Ti-modified support, and the presence of Mo agglomerates over the HAlMCM-41 material. All of these findings indicate that the chemical modification of the MCM-41 material by the substitution of Al for Ti is beneficial for an increase in the proportion of octahedral Mo^{6+} species which are well distributed over the surface of the NiMo catalyst.

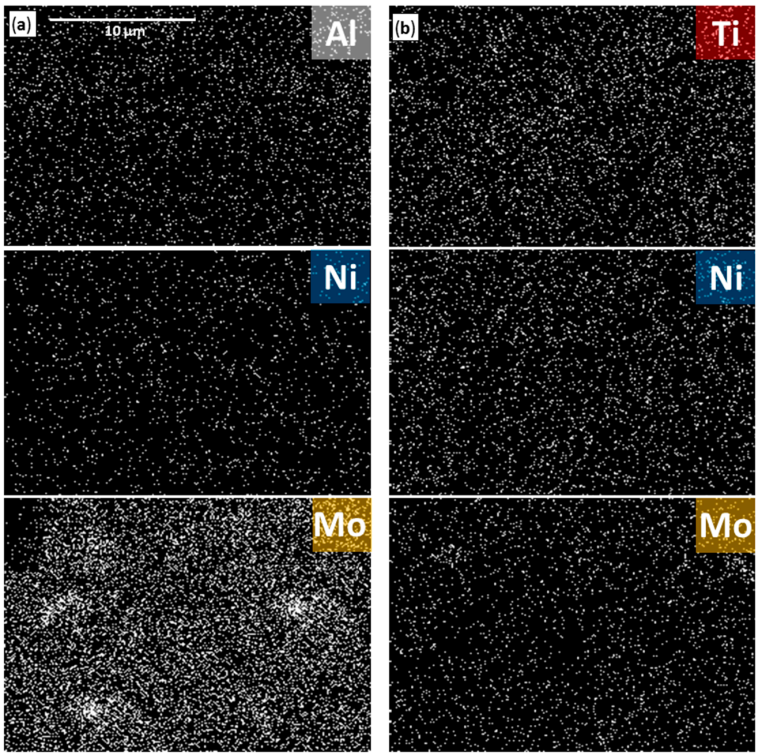

Figure 5. Distribution of Al, Ti, Ni and Mo on the surface of the (**a**) NiMo/HAlMCM-41 and (**b**) NiMo/HTiMCM-41 catalysts.

It is also worth discussing the low degree of sample reduction. Because the sample reduction procedure prior to XPS measurements involved only a 30 min run under a H_2 flow, the effect of the Ni and Mo species' reducibility is insignificant. With a NiMo/HTiMCM-411 H_2-treated catalyst, the results reveal that the peak area of the Ni^0 signal is much smaller than the signals of other Ni-containing species, indicating that only a small fraction of the nickel oxide is reduced. Furthermore, the Mo species are reduced only to a small extent. It should be noted that not only the temperature but also the time affects the reducibility of the NiMo phase. Choi et al. [69] found that after the reduction of MoO_3 at atmospheric pressure and at 500 °C for 3 h, approximately 75% of the total molybdenum was present as Mo^{4+}. Nevertheless, it is evident that the NiMo/HTiMCM-41 sample is more susceptible to reduction than the NiMo/HAlMCM-41 catalyst. To summarize, in this study, the stronger interaction between the Mo species and the HTiMCM-41 support favors the good distribution and activation of the active phase components. The NiMo/HTiMCM-41 catalyst showed interesting catalytic performance, as shown below.

2.4. SEM

The images captured by SEM for the NiMo/HAlMCM-41 and NiMo/HTiMCM-41 catalysts are presented in Figures 5 and 6. The SEM observations (Figure 5) showed the uniformity of the Al and Ti distribution across the surface of the NiMo/HAlMCM-41 and NiMo/HTiMCM-41 catalysts, respectively. As shown by these micrographs, the Ni distribution over NiMo/HTiMCM-41 is slightly more uniform compared to NiMo/HAlMCM-41. The dispersion of Mo over the investigated supports presented even more interesting results. The comparison of the dot mappings for Mo makes it clear that, in the case of NiMo/HAlMCM-41 (Figure 5a), molybdenum is aggregated on the support surface, whereas it is uniformly dispersed on the surface of the NiMo/HTiMCM-41 catalyst (Figure 5b). Thus, it can be concluded that Ti-modification prevents the Mo agglomeration on the catalyst's surface. The coverage of the HTiMCM-41 support with molybdenum is better than HAlMCM-41 because of its stronger MSI. These findings are in line with the XPS results, showing an enhancement of the metal–support interaction in the NiMo/HTiMCM-41 catalyst relative to NiMo/HAlMCM-41.

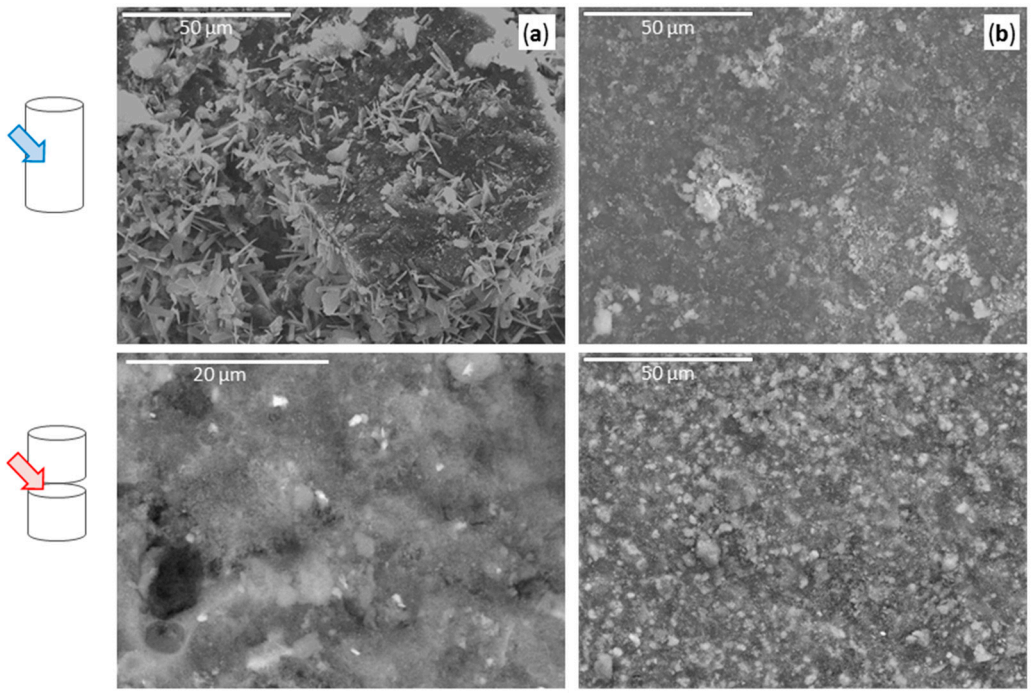

Figure 6. SEM micrographs of the NiMo catalysts: (**a**) NiMo/HAlMCM-41 and (**b**) NiMo/HTiMCM-41 (on the left, the arrow indicates the place of observation on the extrudates).

SEM analyses of the surface morphology by observation of the cylindrical extrudates were carried out on two planes: on the external surface and on the internal plane (i.e., after cracking the drawpiece in half). The SEM images in Figure 6 reveal pronounced differences in the morphology of the catalysts, especially on the external surface of the drawpieces. The SEM image of the surface for the NiMo/HAlMCM-41 catalyst appears to be composed of regular crystallites of various sizes, directed to the surface of the extrudates at different angles (Figure 6a). The crystalline phase occurs as a unique flat-sheet morphology of Mo species, and its density is relatively high. Few agglomerates of Mo have been detected on the internal surface of the NiMo/HAlMCM-41 catalyst. As for NiMo/HTiMCM-41, no crystalline phase of MoO_3 is visible on the external plane (Figure 6b). Only some aggregates of the Mo (fairly dispersed and spread over the layer of the exposed support plane) have been found in this sample. Compared to the NiMo/HAlMCM-41 catalyst, the Mo agglomerates on the surface of the NiMo/HTiMCM-41 are smaller in size. The internal surface of the NiMo/HTiMCM-41 sample is well covered by molybdenum species.

2.5. Catalytic Performance

In order to ascertain the effect of the above features on the HDS activity, hydrodesulfurization experiments on the 4,6-DMDBT and diesel fuel fraction were performed. Figure 7 depicts the relation between the conversion and the contact time (t_c) for the HDS 4,6-DMDBT reaction, and the plots of ln(1/1 − x) against t_c. The results clearly illustrate that the type of support exerts a noticeable influence on the catalytic properties (Figure 7a). In general, a Ti-modified catalyst presents significantly higher HDS activity than the catalyst supported on Al-doped MCM-41. For example, the conversion of 4,6-DMDBT changes with increasing t_c from about 48 to 94% for NiMo/HTiMCM-41, and only from 40 to 88% for NiMo/HAlMCM-41 (Figure 7a); the highest differences are noted within 0.21–0.31 s.

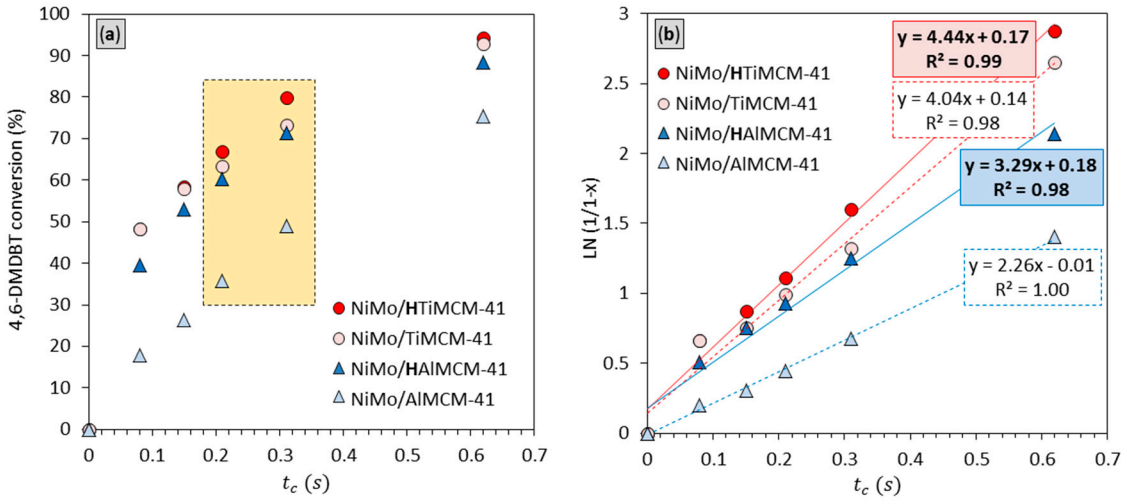

Figure 7. Catalytic performance of NiMo catalysts: (**a**) 4,6-DMDBT conversion (350 °C and 6.0 MPa, t_c in the range 0.08–0.62 s) and (**b**) pseudo-first-order kinetics linear plots for 4,6-DMDBT HDS conversion (ln(1/1 − x) vs. the contact time, where x is the 4,6-DMDBT conversion).

The results show that the 4,6-DMDBT conversion distinctly depends on the modification of the MCM-41 surface with protons. This effect is especially notable over the Al-containing MCM-41 supports. The conversion of 4,6-DMDBT changes with increasing t_c from about 46 to 88% for NiMo/HAlMCM-41, but only from 18 to 75% for NiMo/AlMCM-41 (Figure 7a). The hydrodesulfurization reaction was found to be pseudo-first-order with respect to 4,6-DMDBT over all of the catalysts investigated (Figure 7b). The rate constant value calculated for the HTiMCM-41-based catalyst is 1.3-fold higher than for HAlMCM-41 (Table 4). It is worth noticing that the modification with H^+ of the support's surface yields the catalysts (NiMo/HTiMCM-41 and NiMo/HAlMCM-41), which show higher

rate constant values by 1.1 and 1.5-fold compared to their non-ion-exchanged counterparts (NiMo/TiMCM-41 and NiMo/AlMCM-41), respectively.

Table 4. Activity of NiMo catalysts in the hydrodesulfurization of 4,6-DMDBT.

Catalyst	$k_{4,6\text{-}DMDBT}$ [a]	Conversion (%)	Product Distribution (mol%) [b]				
			MCHT 	3,3′-DMBPh 	3,4′-DMBPh 	4,6-DMTHDBT 	3,6-DMDBT 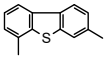
NiMo/HAlMCM-41	3.29	88.3	13.36	66.88	7.09	0.45	0.49
NiMo/AlMCM-41	2.26	75.4	34.75	37.11	*n.d.*	2.60	0.94
NiMo/HTiMCM-41	4.44	94.4	47.86	46.23	*n.d.*	0.14	0.12
NiMo/TiMCM-41	4.04	93.0	65.11	27.17	*n.d.*	0.56	0.12

[a] $k_{4,6-DMDBT}$ overall pseudo-first order rate constant for 4,6-DMDBT hydrodesulfurization; [b] product distribution at the highest 4,6-DMDBT conversion; *n.d.*, not detected.

Summing up, these results show that the incorporation of Ti into the MCM-41 framework (even in the case of a non-proton functionalized catalyst) increases the activity of the NiMo catalysts compared to their Ti-free counterparts. Among all of the catalysts tested, NiMo/HTiMCM-41 displays the highest activity, which was ascribed to important features such as its acidity, active phase dispersion, morphology, and susceptibility to reduction. The incorporation of Ti into the support provides a stronger MSI, allowing an improved dispersion of the Ni and especially Mo oxides (see the SEM images in Figure 5b). In general terms, the high activity of the HDS catalyst may be attributed to the Ni-Mo-S active sites in the so-called Type II morphology that are present after the sulfidation step in NiMo/HTiMCM-41 [70]. The multilayer Ni-Mo-S particles are usually regarded as Type II active phase, which are considered to be more active than the low degree of stacking Type I phase. The Type I morphology of the Ni-Mo-S clusters is characteristic for γ-Al_2O_3 supported catalysts. It is highly probable that in the NiMo/HTiMCM-41 catalyst, the designed preparation procedure, i.e., the introduction of Ti and ion exchange, allows the increase of its reducibility and further sulfidation, improving the formation of multilayer Ni-Mo-S Type II active species. Besides this, the incorporation of Ti can promote the activation of NiMo species, which could be clarified by the fact that, in NiMo/HTiMCM-41, the formation of strong Mo–O–Al and Ni–O–Al linkages is prevented effectively. Therefore, the lower activity of NiMo/HAlMCM-41 (compared to NiMo/HTiMCM-41) can be associated with MSI in an HAlMCM-41-supported catalyst, leading to the formation of $Al_2(MoO_4)_3$ and a nickel-distorted spinel-like structure. The presence of such structures makes the reduction and sulfidation of Ni and Mo species more difficult, and consequently diminishes the catalyst activity. These results are in agreement with the XPS results, showing a better reducibility of Mo in NiMo/HTiMCM-41 relative to the NiMo/HAlMCM-41 sample. Therefore, it can be concluded that the incorporation of Ti and ion exchange is beneficial for the HDS activity of the NiMo/HTiMCM-41 catalyst. This is due to an improvement in the dispersion of the active MoS_2 phase, and in the proportion of Mo oxide species which are capable of being activated properly.

Table 4 shows the product distribution at the highest conversion achieved on each of the catalysts, whereas Figure 8 presents the product distributions along with the full range of t_c for both NiMo catalysts supported over ion-exchanged materials.

Figure 1 presents the main products of the HDS of the 4,6-DMDBT molecule, with all of the sulfur-containing compounds on the top horizontal line and the final hydrocarbon products on the bottom line. The analysis of the reaction pathways was made considering 3-(3′methylcyclohexyl)-toluene (MCHT) and 4,6-dimethyltetrahydrodibenzothiophene (4,6-DMTHDBT) as HYD pathway products, 3,3′-dimethylbiphenyl (3,3′-DMBPh) as a DDS product, and 3,4′-dimethylbiphenyl (3,4′-DMBPh) and 3,6-dimethyldibenzothiophene (3,6-DMDBT) as the ISOM products. The course of the HDS of the 4,6-DMDBT reaction through one of the possible paths depends on the nature of the bond between the 4,6-DMDBT

molecule and the active site. The HYD path is recognized to occur by the formation of the π-bond between the aromatic rings of 4,6-DMDBT and the active site, on which the π electrons of the aromatic rings adsorb. Thus, the saturation of the aromatic rings takes priority over the C–S bond cleavage. The DDS route goes by forming the σ-bond between the electron pair of the S atom of the thiophenic ring and the active site, followed by the C–S bond cleavage without the hydrogenation of the aromatic rings. Nevertheless, the formation of the σ-bond between 4,6-DMDBT is faced with the steric hindrance formed by the alkyl group near the S atom, especially over the conventional sulfide catalysts. Therefore, after the adsorption of 4,6-DMDBT on the catalyst's surface, a π-bond is predominantly formed, rather than a σ-bond. Hence, the HDS runs mostly through the HYD pathway, rather than the DDS. Many efforts have been made to modify the properties of the HDS catalyst in order to direct the HDS reaction to one of the paths. The selectivity of HDS has a key impact on the product quality because the HYD pathway provides an aromatics-free fraction, as well as on H_2 consumption, because the less H_2-consuming DDS pathway is cost effective.

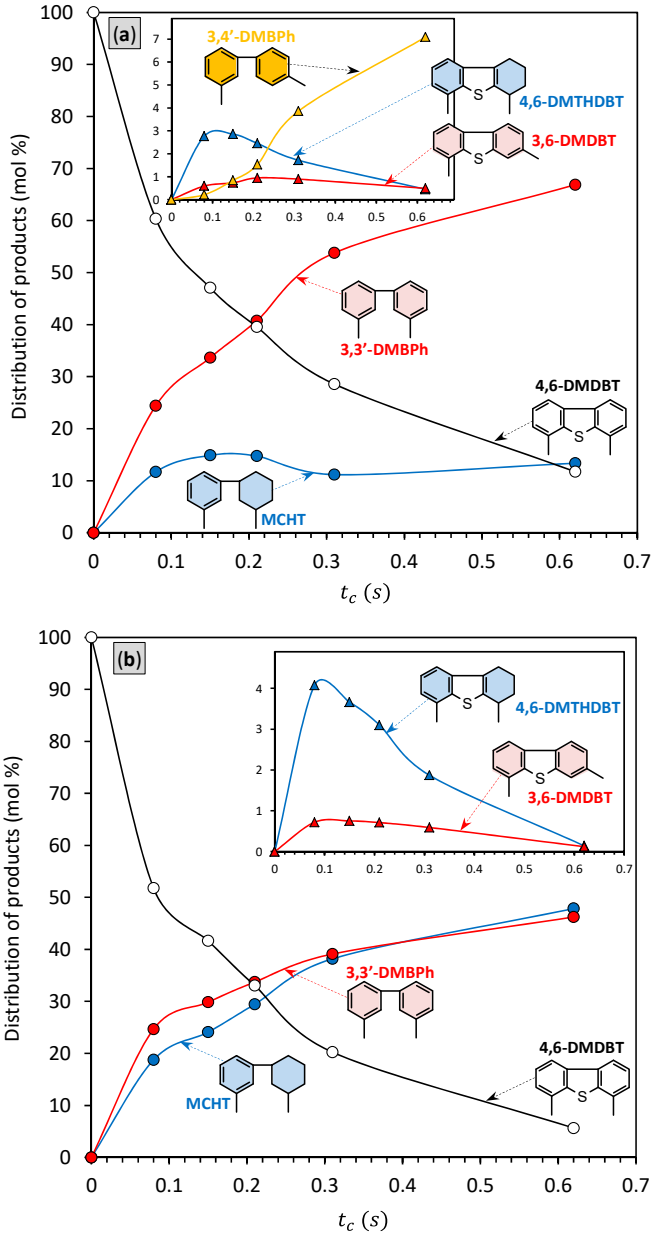

Figure 8. Product distribution for the HDS of 4,6-DMDBT over (**a**) NiMo/HAlMCM-41 and (**b**) NiMo/HTiMCM-41.

Regarding the product distribution over NiMo/HAlMCM-41 (Figure 8a), the main desulfurized product obtained with this catalyst is 3,3′-DMBPh, which shows that the DDS pathway is the predominant HDS reaction route. The NiMo/HAlMCM-41 catalyst unexpectedly shows a high hydrogenolysis ability in HDS of 4,6-DMDBT (the DDS rate with this catalyst was twice as large as that obtained with the NiMo/HTiMCM-41 catalyst). This is in opposite to the privilege of the 4,6-DMDBT molecule for the HYD pathway described above, which is attributed to the hindered action of methyl groups at the positions of 4 and 6, strongly blocking the DDS pathway. However, Esquivel et al. [10] tested NiW/AlSBA15 for 4,6-DMDBT HDS reactions, and reported enhanced activity in the DDS pathway using this support.

From the product distribution plots (Figure 8b) for the NiMo/HTiMCM-41 catalyst, it can be seen that the yield of both 3,3′-DMBPh and MCHT is comparable over the entire range of t_c, and that it increases with increasing t_c. Hence, none of the pathways are the preferred route for the HDS of and 4,6-DMDBT over a HTiMCM-41 supported catalyst. This is contrary to the study by Ganiyu et al. [71] on NiMo/TiSBA-15, which observed that the DDS was the preferred route for the HDS of 4,6-DMDBT. In his work, the HDS rate for DDS was enhanced by the addition of Ti, while the HDS rate for the HYD route remained almost constant. In turn, in the recent work of Morales-Ortuño et al. [72], it was revealed that NiMo catalysts supported on TiSBA-15 and TiSBA-16 desulfurized 4,6-DMDBT principally via the HYD path. It was also reported that the enhanced Mo/TiO_2 catalyst activity enabled a slight increase in the DDS while significantly enhancing the HYD reaction [73].

Considering the HYD/DDS ratio, i.e., the measure of catalyst selectivity (at t_c of 0.62 s), the catalysts can be ordered as follows: NiMo/HAlMCM-41 (0.21) < NiMo/HTiMCM-41 (1.04). This indicates that the Ti-containing catalyst displays a higher hydrogenation capability. This finding is confirmed by the product yield curves shown in Figure 8, where it can be seen that 3,3′-DMBPh is the predominant product for all 4,6-DMDBT conversions for NiMo/HAlMCM-41, whereas over NiMo/HTiMCM-41 the equimolar 3,3′-DMBPh and MCHT product mixture is obtained. Therefore, the results show that the incorporation of Al or Ti into the MCM-41 support, in addition to ion exchange, strongly influences the selectivity of the catalysts for HDS of 4,6-DMDBT.

The NiMo/HAlMCM-41 catalyst shows a relatively high activity together with a significantly lower HYD/DDS ratio than the NiMo/HTiMCM-41 catalyst. This is an interesting finding, because the majority of the catalysts (especially supported over Al-containing materials, e.g., the commercial NiMo/γ-Al_2O_3) which are active for the HDS of 4,6-DMDBT have a high HYD ability. The high HYD selectivity of the catalyst is correlated with the active species morphology, mainly the stacking degree of the MoS_2 phase. It is generally considered that the HYD rate increases with the increasing degree of stacking, which is attributed to the less restricted planar geometry of the adsorption of the reactants on MoS_2 multilayer crystallites [74]. It has been shown that a high activity for HDS 4,6-DMDBT is usually obtained over a catalyst with well-dispersed short (3–4 nm) MoS_2 clusters formed by 2–3 layers. The reduction in the degree of stacking of MoS_2 particles usually resulted in an improvement of the selectivity towards the DDS path and a decrease in the overall catalytic activity of the HDS of alkyl-substituted refractory dibenzothiophenes. Therefore, it can be concluded that, in the case of NiMo/HAlMCM-41, the MSI provides the MoS_2 active species with a low degree of stacking.

In this study, it was found for the first time that the NiMo/HTiMCM-41 system is an effective catalyst displaying high selectivity in HYD, and at the same time in the DDS reaction. The strong interaction between the active species and support in the NiMo/HTiMCM-41 catalyst accounts for a high dispersion, and as a consequence, contributes to the formation of structures which are able to catalyze the HYD reaction. Therefore, the increase in the HYD activity when NiMo/HTiMCM-41 is used may be associated with its increase in the degree of stacking of MoS_2 particles, because this favors the adsorption of 4,6-DMDBT via the π-bond. The acidic properties of the HTiMCM-41 support can also influence the hydrogenation ability of this catalyst. The high activity along with sustained high HYD

activity may be due to the modification of the dispersion and electronic state of the active NiMoS species by the acid centers from the HTiMCM-41 support. Investigating the activity of NiMo/ZSM-5 + SBA-16 [75], Zhou and co-workers inferred that the HDS of DBT mainly proceeds via an HYD route that benefits from the enhanced Brønsted acidity. On the other hand, Shi et al. [76] found that in the NiMo/USNiY catalyst, the dispersion of the metal atoms increases with an increasing concentration of Lewis acid sites, and as a consequence the NiMo/USNiY favors the HYD pathway selectivity in the HDS of 4,6-DMDBT. The other mechanism of HYD over acid sites is based on the spillover hydrogen phenomenon. The study of Lecrenay et al. [77] reported that the addition of an HY zeolite with well-controlled acidity into the $CoMo/Al_2O_3$-HY catalyst provides HYD activity and makes the catalyst more coke resistant. The authors explain the HYD reaction improvement over a $CoMo/Al_2O_3$-HY catalyst in terms of the H-spillover attacking the reaction intermediate formed on some strong acid sites. Hence, the presence of relatively strong Brønsted acid sites and their high concentration in the NiMo/HTiMCM-41 sample may also contribute to the enhancement of its HYD performance.

It is worth noticing that the favorable effect of surface protons introduced in the DDS reaction is evident. Hence, the yield of 3,3′-DMBPh obtained with both NiMo/HAlMCM-41 and NiMo/HTiMCM-41 catalysts at the highest 4,6-DMDBT conversion is almost 2-fold larger than that obtained with its non-ion-exchanged counterparts (Table 4). This should be attributed to an increasing role of the acid sites generated over the surface of ion-exchanged catalysts in the DDS reaction. The acid sites catalyze C–S bond cleavage in the DDS route because they may act as a co-catalyst by providing a proton for facile S-atom removal from the thiophenic ring [78,79]. Hence, the following elimination step of the S^{2-} ions of the active species (acting as basic sites) is easier. The protons located on the sulfur atoms can be relocated to the support surface in order to regenerate the acid sites. This is what also seems to explain the activity of NiMo/HAlMCM-41 and NiMo/HTiMCM-41 in the DDS pathway.

It is worth mentioning that the expected enhancement of the isomerization activity over NiMo/HTiMCM-41 (displaying the highest Brønsted acidity) is not achieved. From among all of the catalysts examined, the NiMo/HAlMCM-41 is the only one showing a significant activity in the isomerization reaction. Even despite the two-fold lower Brønsted acidity than the NiMo/HTiMCM-41 catalyst, the NiMo/HAlMCM-41 brings up to 7 mol % of 3,4′-DMBPh (Figure 8a). Only a small amount of 3,6-DMDBT (which is the intermediate product in the isomerization) is observed on NiMo/HTiMCM-41 (Figure 8b). Therefore, the isomerization activity order between NiMo/HTiMCM-41 and NiMo/HAlMCM-41 cannot be explained only by the trends in the acid sites' concentration; it also involves their strength. The isomerization catalytic activity–acidity correlation observed in this study for the NiMo/HAlMCM-41 catalyst indicates that the isomerization activity is provided by acid sites with moderate strength.

In order to validate the activity of the NiMo catalysts supported on functionalized MCM-41 materials, a diesel fuel fraction with a sulfur content of 0.92 wt% was used as the HDS feed oil (Figure 9). With the temperature applied, the HDS activity of the catalysts increases as follows: NiMo/AlMCM-41 < NiMo/HAlMCM-41 < NiMo/TiMCM-41 < NiMo/HTiMCM-41 (Figure 9a). The activity findings obtained for the HDS tests of diesel fuel are also reflected in the color of the products obtained after hydrotreating (Figure 9b). At 360 °C, the HDS efficiency obtained over the NiMo/HTiMCM-41 catalyst is about 10% higher than that over the NiMo/TiMCM-41 catalyst, and about 14% higher than that in the presence of the NiMo/HAlMCM-41 catalyst. Therefore, in this regard, the real feedstock HDS tests corroborate the results on a model 4,6-DMDBT molecule and the highest activity of NiMo/HTiMCM-41 catalyst. According to a series of HDS tests, it was also found that the influence of the HDS temperature on the sulfur level in the products depends on the catalyst composition. The temperature exerts the highest influence on HDS efficiency when the catalyst is supported over HAlMCM-41 material.

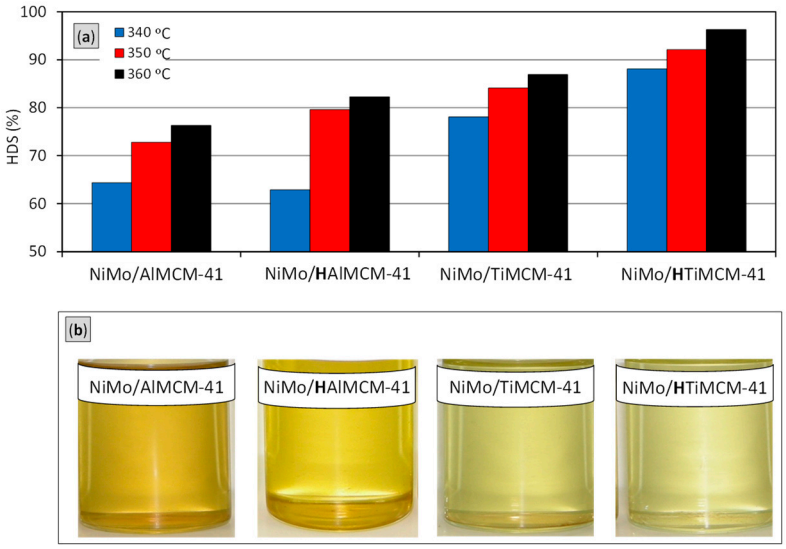

Figure 9. Performance of NiMo catalysts in the HDS of the diesel fuel fraction: (**a**) the effect of the temperature, and (**b**) the products obtained at 360 °C.

The catalytic performance evidences that there is some deviation from the results obtained in the transformation of 4,6-DMDBT. The tendency in promoting the effect of ion exchange on the HDS efficiency is contrary to that obtained in the conversion of the 4,6-DMDBT molecule. More specifically, in the case of Al-containing samples (compare NiMo/AlMCM-41 and NiMo/HAlMCM-41), the ion exchange is concomitant with a slightly greater difference in HDS activity than in the case of Ti-containing ones (compare NiMo/TiMCM-41 and NiMo/HTiMCM-41). This difference in the activities of the catalysts observed in the HDS of the diesel oil fraction and 4,6-DMDBT might be related to the difference in the nature of the feedstocks, and some differences in the activation procedure.

3. Materials and Methods

3.1. Materials

The MCM-41 was synthesized using sodium silicate ($SiO_2 \times NaOH$, 27% SiO_2 in 14% NaOH, Sigma-Aldrich, St. Louis, MO, USA) as a silicon precursor, cetyltrimethylammonium chloride ($CH_3(CH_2)_{15}N(CH_3)_3Cl$, Aldrich) and sulphuric acid (Sigma-Aldrich, 95%). Metal cations were introduced from aluminum(III) sulfate ($Al_2(SO_4)_3 \times 18H_2O$, POCh) and titanium(IV) isopropoxide ($Ti(O_4C_{12}H_{28})$, Honeywell-Fluka, Charlotte, NC, USA). The support extrusion was conducted using aluminium oxyhydroxide as a binder (PURAL KR1, Sasol GmBH; boehmite, S_{BET} = 304 $m^2\ g^{-1}$) and 3% nitric acid(V) (HNO_3, Avantor S.A. Radnor, PA, USA) as a peptising agent. Active ingredients were introduced from a molybdic(VI) acid solution ($H_2MoO_4 \times H_2O$, Avantor S.A.), and nickel was introduced with nickel(II) nitrate ($(Ni(NO_3)_2 \times 6H_2O$, Avantor S.A.). A catalytic test was performed with a reactant mixture of 4,6-DMDBT (Sigma-Aldrich) and decalin (Avantor S.A.). Silicon carbide (SiC, Honeywell-Fluka, Charlotte, NC, USA) was used as an inert material for the catalyst dilution. All of the aqueous solutions were freshly prepared in deionized water.

3.2. Support and Catalyst Preparation

Synthesis of MCM-41: Al- or Ti-substituted MCM-41 materials with a Si/Al (or Si/Ti) ratio of 8 were synthesized following the procedure described by Wojcieszak et al. [52]. In the first step, distilled water (50 g), sulfuric acid (0.3 g) and sodium silicate (8.08 g) were combined under stirring at RT. After 10 min, the template and water mixture (*n*-hexadecyltrimethylammonium chloride, 25 wt% solution in water; 83.75 g) started to be dropped. When half a portion of the template/water mixture was added, the Al or Ti precursor was introduced (1.5130 g of $Al_2(SO_4)_3 \times 18H_2O$ or 1.3439 cm^3 of $Ti(O_4C_{12}H_{28})$),

and in the next step the rest of the surfactant was introduced. The gel obtained was stirred for about half an hour. The pH was adjusted to 11 by the dropwise addition of sulfuric acid with vigorous stirring; after that, 20 g distilled water was added. The gel was loaded into a stoppered PTFE bottle, and it was heated without stirring to 100 °C for 24 h. Next, the mixture was cooled to RT, and the pH was adjusted to 11 by the dropwise addition of sulfuric acid with vigorous stirring. This reaction mixture was heated again to 100 °C for 24 h. The solid obtained was filtered and washed several times with water, and was dried overnight at 100 °C. The template was removed by calcination at 500 °C for 2 h in a helium flow, and 18 h in air. The synthesis of TiMCM-41 was carried out in a dry glove box filled with nitrogen.

Ion exchange: The HAlMCM-41 and HTiMCM-41 materials were obtained from AlMCM-41 and TiMCM-41 by means of an ion exchange procedure using an excess of 0.5 M of a solution of NH_4NO_3. The process was carried out in a reflux system at a temperature of 60 °C for 3 h. Next, the mixture was cooled to 30 °C. The solid was collected by filtration and washed with deionized water after each reaction. The process was repeated until the pH was stabilized, which happened in the third cycle. The protonic form of mesoporous materials was obtained by the thermal decomposition of ammonium ions in the NH4-MCM-41 samples at 550 °C in flowing nitrogen for 2 h and dry air for 4 h.

Preparation of the catalysts: The calcined powders of MCM-41 (non-exchanged and ion-exchanged) were mixed with 10 wt% AlO(OH) (after calcination γ-Al_2O_3), which was used as a binder. The resulting mixtures were peptized with 3% HNO_3 and then shaped into cylindrical pellets using a high-pressure extruder device. The resulting pieces were subjected to drying at 25 °C for 24 h and at 110 °C for 12 h, and then calcination at 500 °C for 3 h. The active ingredients (14 wt% of MoO_3 and 3 wt% of NiO) were added via the two-stage incipient wetness impregnation of the shaped supports. The thermal treatment of the bimetallic catalyst was carried out after each impregnation step, and in the same conditions as those for the extruded carriers.

3.3. Characterization of Supports and Catalysts

Texture and structure: The textural properties of the materials were measured by nitrogen adsorption at −196 °C, using an Autosorb-1C Quantachrome analyzer. Prior to the adsorption measurements, the samples were degassed in vacuum at 150 °C for 12 h (analysis time 13 h). The total surface area of the samples was determined using a BET model. The distribution of the pore sizes was calculated according to the Barrett-Joyner-Halenda method (BJH). The powder XRD data of the samples were recorded in a TUR-62 diffractometer with CuKα radiation, at a scan rate 0.02 2θ/s, within a range of 2θ of 1.4–10°. The mesoporous structure was investigated with a Philips CM-20 SuperTwin TEM microscope, operating at 160 kV and providing 0.25 nm resolution. The samples were prepared by dispersion in methanol and putting a suspension on a microscope copper grid covered with carbon.

Acidity: The acidity, i.e., the type, number and strength of the acid sites, was determined by the adsorption of pyridine (Py–IR). The IR spectra were recorded at room temperature with a BRUKER 48 PC spectrometer. Prior to the acidity measurement via pyridine (Py) chemisorption, the samples were activated at 530 °C for 1 h. The adsorption was carried out at 130 °C, and an excess of pyridine was introduced into the cell. After saturation with Py, the samples were degassed at 130 °C in a vacuum for 30 min. The quantitative calculation of the Brønsted and Lewis acid sites was made with respect to the height of the absorption bands at ca. 1545 and 1455 cm^{-1}, respectively. The integrated absorbance of each band was achieved using suitable software, and the calculation of the adequate acid site number was established using the molar extinction coefficients of $\varepsilon_{1545} \approx 0.07$ cm^2 μmol^{-1} and $\varepsilon_{1455} \approx 0.100$ cm^2 μmol^{-1}. The acid strength distribution was determined on the basis of pyridine desorption studies at elevated temperatures under vacuum conditions. The conservation of the 1545 cm^{-1} (Brønsted sites) and 1455–1440 cm^{-1} (Lewis sites) bands

under the desorption treatment at a temperature of 260 °C was taken as a measure of the strength of the acid sites (A_{260}/A_0).

SEM: The scanning electron microscopy observations were carried out using a Jeol JSM 5888 LV electron microscope equipped with an Oxford Isis system for microanalysis. Prior to the analysis, the samples were sprayed with an approximately 100 nm-thick carbon layer.

XPS: The XPS measurements were performed using a SPECS PHOIBOS 100 hemispherical analyzer equipped with a Mg source (1253.6 eV) operating at 100 W (wide-range scan) and 200 W (high-resolution spectra). The spectrometer energy scale was calibrated with the use of Au $4f_{7/2}$, Ag $3d_{5/2}$, and Cu $2p_{3/2}$ lines at 84.2 eV, 367.9 eV and 932.4 eV, respectively. The analyzer mode was set at a constant pass energy of 30 eV in the survey, and 5 eV in the narrow scans. The detection angle was normal to the sample surface. The base pressure in the UHV analysis chamber was better than 5×10^{-10} mbar. The correction of the energy shift due to the static charging of the samples was accomplished with a C 1s peak at 284.6 eV as a reference. The spectra were collected and processed using SpecsLab software. The accuracy of the reported binding energies was ±0.1 eV. The element concentrations were evaluated from the peak areas after Shirley background subtraction.

3.4. Catalytic Activity Assessment

The reactions were carried out in a continuous-flow microreactor. The catalyst was crushed and sieved to a particle size of 0.25–0.315 mm. A sample of 0.5 g catalyst diluted with 2.5 g SiC was used for each reaction. The catalyst was presulfided in situ with a mixture of 2.5 wt% dimethyldisulfide in decaline at 350 °C and 6.0 MPa for 4 h. The liquid reactant (4,6-DMDBT in decaline, 300 ppm S) was fed to the reactor by means of a high-pressure pump. The catalytic activity was determined at 350 °C, 6.0 MPa. The contact time (t_c = 0.08−0.62 s) was changed by varying the flow rates of the liquid and the gaseous reactants while keeping their ratio constant. The catalyst was stabilized for a minimum of 3 h after the contact times were changed. The reaction products were collected at the reactor outlet every hour, and were analyzed by a gas chromatograph equipped with a 30-m HP–1 capillary column (30 m × 0.25 mm × 0.25 μm) and a flame ionization detector.

The conversion (*Conv.*) of 4,6-DMDBT and the degree of the HDS of 4,6-DMDBT were defined by the following:

$$Conv.\,of\ 4,6\text{-}DMDBT = \frac{S_s}{S_S + S_{4,6\text{-}DMDBT}} \times 100\%$$

$$Degree\,of\ HDS = \frac{S_H}{S_S + S_{4,6\text{-}DMDBT}} \times 100\%$$

where S_s is the sum of the molar % of all of the products formed after the catalytic transformation of 4,6-DMDBT (including sulfur-containing compounds). $S_{4,6D\text{-}MDBT}$ is the molar % of 4,6-DMDBT still present after the reaction. S_H is the sum of the molar % of all of the non-sulfur-containing products formed after the catalytic transformation of 4,6-DMDBT. The contact time (t_c) was defined as follows:

$$t_C(s) = \frac{Catalyst\ volume\ (\mathrm{cm}^3)}{(H_2\ flow + Feed\ flow)(\mathrm{cm}^3\ \mathrm{s}^{-1})}$$

The *HDS* of a diesel oil fraction containing 0.92 wt% *S* (density, 864 kg m^{-3}; IBP, 231 °C; FBP, 375 °C; $T_{360°C}$ = 90 vol.%) was carried out in a high-pressure flow fixed-bed reactor (temperature, 340–360 °C; pressure, 6 MPa; LSHV, 3 h^{-1}; H_2, feed ratio, 350:1 Nm^3/m^3). Before the activity measurements, the catalyst (4 cm^3, with a grain size of 0.75–1.02 mm) was activated via the following procedure: reduction (H_2 pressure of 6 MPa, 340 °C, 2 h) followed by sulfidation, using a diesel oil fraction (*S*, 0.92 wt%) at 350 °C, 6 MPa, 3 h^{-1}, 350:1 Nm^3/m^3. The sulfur concentrations in the feed and products were analyzed by XRD fluorescence spectroscopy (Phillips PW 1400).

4. Conclusions

This investigation attempted to determine the ways in which the modification of the MCM-41 sieves with Al- or Ti-substitution and proton incorporation affects the properties and activity of NiMo catalysts shaped with a binder. The activity of catalytic systems of NiMo/HAlMCM-41 and NiMo/HTiMCM-41 was compared in the HDS of 4,6-dimethyldibenzothiophene (4,6-DMDBT) and diesel fuel with a 0.92 wt% sulfur concentration. It was found that the Ti-containing materials (HTiMCM-41 and NiMo/HTiMCM-41) exhibited much better textural properties, acidity and metal–support interactions than their Al-containing counterparts (HAlMCM-41 and NiMo/HAlMCM-41). The functionalization of mesoporous materials with protons via ion exchange enhanced significantly the catalytic activity of NiMo/HAlMCM-41 and NiMo/HTiMCM-41 catalysts in the HDS reaction. The catalyst selectivity with respect to the reaction path (DDS or HYD) was determined by the ratio of the number of Brønsted to Lewis centers. It was evident that the NiMo/HTiMCM-41 catalyst displayed the most promising catalytic properties for the HDS, relative to NiMo/HAlMCM-41 and to the two other non-ion-exchanged catalysts (NiMo/AlMCM-41 and NiMo/TiMCM-41). In this study, for the first time, we have achieved an NiMo/HTiMCM-41 catalytic system, in the molded form (drawpieces) characteristic of industrial catalysts, showing superior performance in the HDS of 4,6-DMDBT and the diesel fuel fraction due to some mutual effects: (i) an adequate surface area ensuring the good dispersion of the active metals, (ii) the high acidity making the catalyst active in both the HYD and DDS pathways, and (iii) the metal–support interaction providing the multilayered stacking of the active phase and the high dispersion of Ni–Mo–S slabs. As a result, the synergistic effects of the physicochemical features of the NiMo/HTiMCM-41 catalyst, the susceptibility to sulfidation, and metal–support interaction of the active metallic species coordinately contribute to the catalytic performance in the HDS of 4,6-DMDBT and real diesel fuel feedstock. Nevertheless, a more detailed study of the activated (i.e., sulfided) and spent NiMo catalysts supported on the HAlMCM-41 and HTiMCM-41 materials is required in order to explain the reasons for the strong modification in the catalytic activity. Moreover, further studies are required to show the performance of the mesoporous catalysts in the long reaction time in a stream test.

Author Contributions: Conceptualization, K.J. and J.G.; Methodology, K.J., M.L., K.G.-M. and G.D.-M.; Software, K.J.; Validation, K.J., M.L., K.G.-M. and G.D.-M.; Formal analysis, K.J., M.L., K.G.-M. and G.D.-M., Investigation, K.J., M.L. and K.G.-M.; Resources; K.J.; Data curation, K.J., M.L. and K.G.-M.; Writing—original draft preparation, K.J.; Writing—review and editing, K.J., M.L. and K.G.-M.; Visualization, K.J.; Supervision, K.J. and J.G.; Project administration, K.J. and J.G.; Funding acquisition, K.J. and J.G. All authors have read and agreed to the published version of the manuscript.

Funding: The work was supported by a statutory activity subsidy (2021) from the Ministry of Science and Higher Education, Republic of Poland, for the Faculty of Chemistry of Wrocław University of Science and Technology. K.J. would like to thank the Ministry of Science and Higher Education, Republic of Poland, for the financial support through its T09B 112 26 project.

Institutional Review Board Statement: Not applicable.

Informed Consent Statement: Not applicable.

Data Availability Statement: The authors confirm that the data supporting the findings of this study are available within the article.

Acknowledgments: Sasol is acknowledged for providing the alumina binder.

Conflicts of Interest: The authors declare that they have no known competing financial interest or personal relationships that could have appeared to influence the work reported in this paper.

References

1. Alotaibi, F.M.; González-Cortés, S.; Alotibi, M.F.; Xiao, T.; Al-Megren, H.; Yang, G.; Edwards, P.P. Enhancing the production of light olefins from heavy crude oils: Turning challenges into opportunities. *Catal. Today* **2018**, *317*, 86–98. [CrossRef]
2. Trongkaew, P.; Utistham, T.; Reubroycharoen, P.; Hinchiranan, N. Photocatalytic desulfurization of waste tire pyrolysis oil. *Energies* **2011**, *4*, 1880–1896. [CrossRef]
3. Pieterse, J.A.Z.; Van Eijk, S.; Van Dijk, H.A.J.; Van Den Brink, R.W. On the potential of absorption and reactive adsorption for desulfurization of ultra low-sulfur commercial diesel in the liquid phase in the presence of fuel additive and bio-diesel. *Fuel Process. Technol.* **2011**, *92*, 616–623. [CrossRef]
4. Stanislaus, A.; Marafi, A.; Rana, M.S. Recent advances in the science and technology of ultra low sulfur diesel (ULSD) production. *Catal. Today* **2010**, *153*, 1–68. [CrossRef]
5. Shamsaee, B.H.; Mehri, F.; Rowshanzamir, S.; Ghamati, M.; Behrouzifar, A. Desulfurization of benzothiophene from model diesel fuel using experimental (dynamic electroreduction) and theoretical (DFT) approaches. *Sep. Purif. Technol.* **2019**, *212*, 505–514. [CrossRef]
6. Tanimu, A.; Alhooshani, K. Advanced Hydrodesulfurization Catalysts: A Review of Design and Synthesis. *Energy Fuels* **2019**, *33*, 2810–2838. [CrossRef]
7. Bej, S.K.; Maity, S.K.; Turaga, U.T. Catalyst: A Review of Recent Studies. *Energy Fuels* **2005**, *18*, 1227. [CrossRef]
8. Hossain, M.N.; Park, H.C.; Choi, H.S. A comprehensive review on catalytic oxidative desulfurization of liquid fuel oil. *Catalysts* **2019**, *9*, 229. [CrossRef]
9. Cao, Z.; Zhang, X.; Guo, R.; Ding, S.; Zheng, P.; Fan, J.; Mei, J.; Xu, C.; Duan, A. Synergistic effect of acidity and active phases for NiMo catalysts on dibenzothiophene hydrodesulfurization performance. *Chem. Eng. J.* **2020**, *400*, 125886. [CrossRef]
10. Esquivel, G.M.; Ramírez, J.; Gutiérrez-Alejandre, A. HDS of 4,6-DMDBT over NiW/Al-SBA15 catalysts. *Catal. Today* **2010**, *148*, 36–41. [CrossRef]
11. Alonso-Pérez, M.O.; Pawelec, B.; Zepeda, T.A.; Alonso-Núñez, G.; Nava, R.; Navarro, R.M.; Huirache-Acuña, R. Effect of the titanium incorporation method on the morphology and HDS activity of supported ternary Ni–Mo–W/SBA-16 catalysts. *Microporous Mesoporous Mater.* **2021**, *312*, 110779. [CrossRef]
12. Luo, Q.; Zhou, Q.; Lin, Y.; Wu, S.; Liu, H.; Du, C.; Zhong, Y.; Yang, C. Fast and deep oxidative desulfurization of dibenzothiophene with catalysts of MoO_3-TiO_2@MCM-22 featuring adjustable Lewis and Brønsted acid sites. *Catal. Sci. Technol.* **2019**, *9*, 6166–6179. [CrossRef]
13. Han, W.; Nie, H.; Long, X.; Li, M.; Yang, Q.; Li, D. Effects of the support BrØnsted acidity on the hydrodesulfurization and hydrodenitrogention activity of sulfided NiMo/Al_2O_3 catalysts. *Catal. Today* **2017**, *292*, 58–66. [CrossRef]
14. Brunet, S.; Lebeau, B.; Naboulsi, I.; Michelin, L.; Comparot, J.D.; Marichal, C.; Rigolet, S.; Bonne, M.; Blin, J. Effect of Mesostructured Zirconia Support on the Activity and Selectivity of 4,6-Dimethydibenzothiophene Hydrodesulfurization. *Catalysts* **2020**, *10*, 1162. [CrossRef]
15. Liu, H.; Li, Y.; Yin, C.; Wu, Y.; Chai, Y.; Dong, D.; Li, X.; Liu, C. One-pot synthesis of ordered mesoporous NiMo-Al2O3 catalysts for dibenzothiophene hydrodesulfurization. *Appl. Catal. B Environ.* **2016**, *198*, 493–507. [CrossRef]
16. Huirache-Acuña, R.; Pérez-Ayala, E.; Cervantes-Gaxiola, M.E.; Alonso-Nuñez, G.; Zepeda, T.A.; Rivera-Muñoz, E.M.; Pawelec, B. Dibenzothiophene hydrodesulfurization over ternary metallic NiMoW/Ti-HMS mesoporous catalysts. *Catal. Commun.* **2021**, *148*, 106162. [CrossRef]
17. Méndez, F.J.; Franco-López, O.E.; Bokhimi, X.; Solís-Casados, D.A.; Escobar-Alarcón, L.; Klimova, T.E. Dibenzothiophene hydrodesulfurization with NiMo and CoMo catalysts supported on niobium-modified MCM-41. *Appl. Catal. B Environ.* **2017**, *219*, 479–491. [CrossRef]
18. Méndez, F.J.; Franco-López, O.E.; Díaz, G.; Gómez-Cortés, A.; Bokhimi, X.; Klimova, T.E. On the role of niobium in nanostructured Mo/Nb-MCM-41 and NiMo/Nb-MCM-41 catalysts for hydrodesulfurization of dibenzothiophene. *Fuel* **2020**, *280*, 118550. [CrossRef]
19. Rauscher, T.; Müller, C.I.; Schmidt, A.; Kieback, B.; Röntzsch, L. Ni-Mo-B alloys as cathode material for alkaline water electrolysis. *Int. J. Hydrogen Energy* **2016**, *41*, 2165–2176. [CrossRef]
20. Jaroszewska, K.; Lewandowski, M.; Grzechowiak, J.R.; Szyja, B. Author's personal copy Hydrodesulphurisation of 4, 6-dimethyldibenzothiophene over NiMo catalysts supported on Ti (Al) modified MCM-41. *Catal. Today* **2011**, *176*, 202–207. [CrossRef]
21. Nava, R.; Ortega, R.A.; Alonso, G.; Ornelas, C.; Pawelec, B.; Fierro, J.L.G. CoMo/Ti-SBA-15 catalysts for dibenzothiophene desulfurization. *Catal. Today* **2007**, *127*, 70–84. [CrossRef]
22. Wang, A.; Wanga, Y.; Chen, Y.; Li, X.; Yao, P.; Kabe, T. Hydrodesulfurization of dibenzothiophene over Mo-based catalysts supported by siliceous MCM-41. *Stud. Surf. Sci. Catal.* **2002**, *142*, 795–798. [CrossRef]
23. Wang, A.; Li, X.; Wang, Y.; Sun, Z.; Li, C.; Hu, Y. Hydrodesulfurizatton of dibenzothiophene over proton-exchanged siliceous MCM-41 supported bimetallic sulfides. In *Studies in Surface Science and Catalysis*; Elsevier: Amsterdam, The Netherlands, 2004; Volume 154, pp. 2930–2935.
24. Trejda, M.; Ziolek, M. New iron containing mesoporous catalysts. *Catal. Today* **2005**, *101*, 109–116. [CrossRef]
25. Sluban, M.; Cojocaru, B.; Parvulescu, V.I.; Iskra, J.; Cerc Korošec, R.; Umek, P. Protonated titanate nanotubes as solid acid catalyst for aldol condensation. *J. Catal.* **2017**, *346*, 161–169. [CrossRef]

26. Camposeco, R.; Castillo, S.; Mejia-Centeno, I.; Navarrete, J.; Rodriguez-Gonzalez, V. Behavior of Lewis and Brönsted surface acidity featured by Ag, Au, Ce, La, Fe, Mn, Pd, Pt, V and W decorated on protonated titanate nanotubes. *Microporous Mesoporous Mater.* **2016**, *236*, 235–243. [CrossRef]
27. Vutolkina, A.V.; Glotov, A.P.; Zanina, A.V.; Makhmutov, D.F.; Maximov, A.L.; Egazar'yants, S.V.; Karakhanov, E.A. Mesoporous Al-HMS and Al-MCM-41 supported Ni-Mo sulfide catalysts for HYD and HDS via in situ hydrogen generation through a WGSR. *Catal. Today* **2019**, *329*, 156–166. [CrossRef]
28. Cánepa, A.L.; Vaschetti, V.M.; Pájaro, K.C.; Eimer, G.A.; Casuscelli, S.G.; Cortés Corberán, V. Selective oxidation of ethanol on V-MCM-41 catalysts. *Catal. Today* **2020**, *356*, 464–470. [CrossRef]
29. Kwak, K.Y.; Kim, M.S.; Lee, D.W.; Cho, Y.H.; Han, J.; Kwon, T.S.; Lee, K.Y. Synthesis of cyclopentadiene trimer (tricyclopentadiene) over zeolites and Al-MCM-41: The effects of pore size and acidity. *Fuel* **2014**, *137*, 230–236. [CrossRef]
30. Shestakova, P.; Popova, M.; Szegedi, Á.; Lazarova, H.; Nga Luong, T.K.; Trendafilova, I.; Mihály, J.; Parac-Vogt, T.N. Hybrid catalyst with combined Lewis and Brønsted acidity based on ZrIV substituted polyoxometalate grafted on mesoporous MCM-41 silica for esterification of renewable levulinic acid. *Microporous Mesoporous Mater.* **2021**, *323*, 111203. [CrossRef]
31. Ziaei-Azad, H.; Kolle, J.M.; Al-Yasser, N.; Sayari, A. One-pot synthesis of large-pore AlMCM-41 aluminosilicates with high stability and adjustable acidity. *Microporous Mesoporous Mater.* **2018**, *262*, 166–174. [CrossRef]
32. Araújo, R.S.; Maia, D.A.S.; Azevedo, D.C.S.; Cavalcante, C.L.; Rodríguez-Castellón, E.; Jimenez-Lopez, A. Assessment of surface acidity in mesoporous materials containing aluminum and titanium. *Appl. Surf. Sci.* **2009**, *255*, 6205–6209. [CrossRef]
33. Ng, E.P.; Nur, H.; Wong, K.L.; Muhid, M.N.M.; Hamdan, H. Generation of Brönsted acidity in AlMCM-41 by sulphation for enhanced liquid phase tert-butylation of phenol. *Appl. Catal. A Gen.* **2007**, *323*, 58–65. [CrossRef]
34. Góra-Marek, K.; Datka, J. IR studies of OH groups in mesoporous aluminosilicates. *Appl. Catal. A Gen.* **2006**, *302*, 104–109. [CrossRef]
35. Tekla, J.; Tarach, K.A.; Olejniczak, Z.; Girman, V.; Góra-Marek, K. Effective hierarchization of TS-1 and its catalytic performance in cyclohexene epoxidation. *Microporous Mesoporous Mater.* **2016**, *233*, 16–25. [CrossRef]
36. Wada, E.; Kitano, M.; Nakajima, K.; Hara, M. Effect of preparation conditions on the structural and acid catalytic properties of protonated titanate nanotubes. *J. Mater. Chem. A* **2013**, *1*, 12768–12774. [CrossRef]
37. Li, S.; Li, N.; Li, G.; Li, L.; Wang, A.; Cong, Y.; Wang, X.; Xu, G.; Zhang, T. Protonated titanate nanotubes as a highly active catalyst for the synthesis of renewable diesel and jet fuel range alkanes. *Appl. Catal. B Environ.* **2015**, *170–171*, 124–134. [CrossRef]
38. Kitano, M.; Nakajima, K.; Kondo, J.N.; Hayashi, S.; Hara, M. Protonated Titanate Nanotubes as Solid Acid Catalyst. *J. Am. Chem. Soc.* **2010**, *132*, 6622–6623. [CrossRef]
39. Camposeco, R.; Castillo, S.; Mejía-Centeno, I.; Navarrete, J.; Nava, N.; Rodríguez-González, V. Synthesis of protonated titanate nanotubes tailored by the washing step: Effect upon acid properties and photocatalytic activity. *J. Photochem. Photobiol. A Chem.* **2017**, *341*, 87–96. [CrossRef]
40. Prasad Reddy, B.R.; Govardhana Reddy, P.V.; Kumar, D.P.; Reddy, B.N.; Shankar, M.V. Rapid synthesis of alkylaminophenols via the Petasis borono-Mannich reaction using protonated trititanate nanotubes as robust solid-acid catalysts. *RSC Adv.* **2016**, *6*, 14682–14691. [CrossRef]
41. Kitano, M.; Wada, E.; Nakajima, K.; Hayashi, S.; Miyazaki, S.; Kobayashi, H.; Hara, M. Protonated titanate nanotubes with Lewis and Brønsted acidity: Relationship between nanotube structure and catalytic activity. *Chem. Mater.* **2013**, *25*, 385–393. [CrossRef]
42. Tarach, K.A.; Śrębowata, A.; Kowalewski, E.; Gołąbek, K.; Kostuch, A.; Kruczała, K.; Girman, V.; Góra-Marek, K. Nickel loaded zeolites FAU and MFI: Characterization and activity in water-phase hydrodehalogenation of TCE. *Appl. Catal. A Gen.* **2018**, *568*, 64–75. [CrossRef]
43. Li, M.; Fu, J.; Xing, S.; Yang, L.; Zhang, X.; Lv, P.; Wang, Z.; Yuan, Z. A novel catalyst with variable active sites for the direct hydrogenation of waste oils into jet fuel. *Appl. Catal. B Environ.* **2020**, *260*, 118114. [CrossRef]
44. Navajas, A.; Jim, E.; Romero-sarria, F. Molybdenum Oxide for the Production of Biodiesel from Oil with High Free Fatty Acids Content. 1–14. *Catalysts* **2020**, *10*, 158. [CrossRef]
45. Lakiss, L.; Gilson, J.P.; Valtchev, V.; Mintova, S.; Vicente, A.; Vimont, A.; Bedard, R.; Abdo, S.; Bricker, J. Zeolites in a good shape: Catalyst forming by extrusion modifies their performances. *Microporous Mesoporous Mater.* **2020**, *299*. [CrossRef]
46. Zaki, M.I.; Hasan, M.A.; Al-Sagheer, F.A.; Pasupulety, L. In situ FTIR spectra of pyridine adsorbed on SiO_2-Al_2O_3, TiO_2, ZrO_2 and CeO_2: General considerations for the identification of acid sites on surfaces of finely divided metal oxides. *Colloids Surf. A Physicochem. Eng. Asp.* **2001**, *190*, 261–274. [CrossRef]
47. Martin, C.; Martin, I.; Delmoral, C.; Rives, V. FT-IR Assessment Through Pyridine Adsorption of the Surface Acidity of Alkali-Doped MoO_3/TiO_2. *J. Catal.* **1994**, *146*, 415–421. [CrossRef]
48. Daoura, O.; Fornasieri, G.; Boutros, M.; El Hassan, N.; Beaunier, P.; Thomas, C.; Selmane, M.; Miche, A.; Sassoye, C.; Ersen, O.; et al. One-pot prepared mesoporous silica SBA-15-like monoliths with embedded Ni particles as selective and stable catalysts for methane dry reforming. *Appl. Catal. B Environ.* **2021**, *280*, 119417. [CrossRef]
49. Shi, L.Y.; Li, Y.X.; Xue, D.M.; Tan, P.; Jiang, Y.; Liu, X.Q.; Sun, L.B. Fabrication of highly dispersed nickel in nanoconfined spaces of as-made SBA-15 for dry reforming of methane with carbon dioxide. *Chem. Eng. J.* **2020**, *390*, 124491. [CrossRef]
50. Fang, K.; Ren, J.; Sun, Y. Effect of nickel precursors on the performance of Ni/AlMCM-41 catalysts for n-dodecane hydroconversion. *J. Mol. Catal. A Chem.* **2005**, *229*, 51–58. [CrossRef]

51. Lim, Z.Y.; Ma, X.; Chen, B. Enhanced porosity of Ni@HSZ for dry reforming of methane. *New J. Chem.* **2020**, *44*, 1707–1710. [CrossRef]
52. Wojcieszak, R.; Monteverdi, S.; Mercy, M.; Nowak, I.; Ziolek, M.; Bettahar, M.M. Nickel containing MCM-41 and AlMCM-41 mesoporous molecular sieves: Characteristics and activity in the hydrogenation of benzene. *Appl. Catal. A Gen.* **2004**, *268*, 241–253. [CrossRef]
53. Afshar Taromi, A.; Kaliaguine, S. Hydrodeoxygenation of triglycerides over reduced mesostructured Ni/Γ-alumina catalysts prepared via one-pot sol-gel route for green diesel production. *Appl. Catal. A Gen.* **2018**, *558*, 140–149. [CrossRef]
54. Patil, R.B.; House, S.D.; Mantri, A.; Yang, J.C.; McKone, J.R. Direct Observation of Ni-Mo Bimetallic Catalyst Formation via Thermal Reduction of Nickel Molybdate Nanorods. *ACS Catal.* **2020**, *10*, 10390–10398. [CrossRef]
55. Wang, F.; Yu, F.; Wei, Y.; Li, A.; Xu, S.; Lu, X. Promoting hydrocarbon production from fatty acid pyrolysis using transition metal or phosphorus modified Al-MCM-41 catalyst. *J. Anal. Appl. Pyrolysis* **2021**, *156*, 105146. [CrossRef]
56. Afshar Taromi, A.; Kaliaguine, S. Green diesel production via continuous hydrotreatment of triglycerides over mesostructured Γ-alumina supported NiMo/CoMo catalysts. *Fuel Process. Technol.* **2018**, *171*, 20–30. [CrossRef]
57. Cortés, J.C.; Rodríguez, C.; Molina, R.; Moreno, S. Hydrocracking of 1-methylnaphtalene (1MN) over modified clays-supported NiMoS and NiWS catalyst. *Fuel* **2021**, *295*, 120612. [CrossRef]
58. Chong, C.C.; Bukhari, S.N.; Cheng, Y.W.; Setiabudi, H.D.; Jalil, A.A.; Phalakornkule, C. Robust Ni/Dendritic fibrous SBA-15 (Ni/DFSBA-15) for methane dry reforming: Effect of Ni loadings. *Appl. Catal. A Gen.* **2019**, *584*, 117174. [CrossRef]
59. Gundeboina, R.; Gadasandula, S.; Velisoju, V.K.; Gutta, N.; Kotha, L.R.; Aytam, H.P. Ni-Al-Ti Hydrotalcite Based Catalyst for the Selective Hydrogenation of Biomass-Derived Levulinic Acid to γ-Valerolactone. *ChemistrySelect* **2019**, *4*, 202–210. [CrossRef]
60. Ganiyu, S.A.; Ali, S.A.; Alhooshani, K. Synthesis of a Ti-SBA-15-nimo hydrodesulfurization catalyst: The effect of the hydrothermal synthesis temperature of nimo and molybdenum loading on the catalytic activity. *Ind. Eng. Chem. Res.* **2017**, *56*, 5201–5209. [CrossRef]
61. Cao, Y.; Wang, H.; Ding, R.; Wang, L.; Liu, Z.; Lv, B. Highly efficient oxidative desulfurization of dibenzothiophene using Ni modified MoO_3 catalyst. *Appl. Catal. A Gen.* **2020**, *589*. [CrossRef]
62. Puello-Polo, E.; Pájaro, Y.; Márquez, E. Effect of the Gallium and Vanadium on the Dibenzothiophene Hydrodesulfurization and Naphthalene Hydrogenation Activities Using Sulfided NiMo-V_2O_5/Al_2O_3-Ga_2O_3. *Catalysts* **2020**, *10*, 894. [CrossRef]
63. Méndez, F.J.; Bravo-Ascención, G.; González-Mota, M.; Puente-Lee, I.; Bokhimi, X.; Klimova, T.E. NiMo catalysts supported on Al, Nb, Ti or Zr-containing MCM-41 for dibenzothiophene hydrodesulfurization. *Catal. Today* **2020**, *349*, 217–227. [CrossRef]
64. Zepeda, T.A.; Pawelec, B.; Fierro, J.L.G.; Halachev, T. Effect of Ti on the catalytic properties of CoMo/Ti(x)-HMS catalysts in the reaction of hydrodesulfurization of 4-ethyl-6-methyl dibenzothiophene. *J. Catal.* **2006**, *242*, 254–269. [CrossRef]
65. Klimova, T.; Reyes, J.; Gutiérrez, O.; Lizama, L. Novel bifunctional NiMo/Al-SBA-15 catalysts for deep hydrodesulfurization: Effect of support Si/Al ratio. *Appl. Catal. A Gen.* **2008**, *335*, 159–171. [CrossRef]
66. Gao, Q.; Zhang, Y.; Zhou, K.; Wu, H.; Guo, J.; Zhang, L.; Duan, A.; Zhao, Z.; Zhang, F.; Zhou, Y. Synthesis of ZSM-5/KIT-6 with a tunable pore structure and its catalytic application in the hydrodesulfurization of dibenzothiophene and diesel oil. *RSC Adv.* **2018**, *8*, 28879–28890. [CrossRef]
67. Tio, S.; Reddy, B.M.; Chowdhury, B.; Smirniotis, P.G. An XPS study of the dispersion of MoO_3 on. *Appl. Catal.* **2001**, *211*, 19–30.
68. Vozka, P.; Orazgaliyeva, D.; Šimáček, P.; Blažek, J.; Kilaz, G. Activity comparison of Ni-Mo/Al_2O_3 and Ni-Mo/TiO_2 catalysts in hydroprocessing of middle petroleum distillates and their blend with rapeseed oil. *Fuel Process. Technol.* **2017**, *167*, 684–694. [CrossRef]
69. Choi, J.G.; Thompson, L.T. XPS study of as-prepared and reduced molybdenum oxides. *Appl. Surf. Sci.* **1996**, *93*, 143–149. [CrossRef]
70. Zhou, W.; Yang, L.; Liu, L.; Chen, Z.; Zhou, A.; Zhang, Y.; He, X.; Shi, F.; Zhao, Z. Synthesis of novel NiMo catalysts supported on highly ordered TiO_2-Al_2O_3 composites and their superior catalytic performance for 4,6-dimethyldibenzothiophene hydrodesulfurization. *Appl. Catal. B Environ.* **2020**, *268*, 118428. [CrossRef]
71. Ganiyu, S.A.; Ali, S.A.; Alhooshani, K. Simultaneous HDS of DBT and 4,6-DMDBT over single-pot Ti-SBA-15-NiMo catalysts: Influence of Si/Ti ratio on the structural properties, dispersion and catalytic activity. *RSC Adv.* **2017**, *7*, 21943–21952. [CrossRef]
72. Morales-Ortuño, J.C.; Ortega-Domínguez, R.A.; Hernández-Hipólito, P.; Bokhimi, X.; Klimova, T.E. HDS performance of NiMo catalysts supported on nanostructured materials containing titania. *Catal. Today* **2016**, *271*, 127–139. [CrossRef]
73. Castillo-Villalón, P.; Ramírez, J.; Cuevas, R.; Vázquez, P.; Castañeda, R. Influence of the support on the catalytic performance of Mo, CoMo, and NiMo catalysts supported on Al_2O_3 and TiO_2 during the HDS of thiophene, dibenzothiophene, or 4,6-dimethyldibenzothiophene. *Catal. Today* **2016**, *259*, 140–149. [CrossRef]
74. Hensen, E.J.M.; Kooyman, P.J.; Van der Meer, Y.; Van der Kraan, A.M.; De Beer, V.H.J.; Van Veen, J.A.R.; Van Santen, R.A.; Kooyman, P.J.; Van der Meer, Y.; Van der Kraan, A.M. The relation between morphology and hydrotreating activity for supported MoS_2 particles. *J. Catal.* **2001**, *199*, 224–235. [CrossRef]
75. Zhou, W.; Liu, M.; Zhou, Y.; Wei, Q.; Zhang, Q.; Ding, S.; Zhang, Y.; Yu, T.; You, Q. 4,6-Dimethyldibenzothiophene Hydrodesulfurization on Nickel-Modified USY-Supported NiMoS Catalysts: Effects of Modification Method. *Energy Fuels* **2017**, *31*, 7445–7455. [CrossRef]

76. Shi, Y.; Wang, G.; Mei, J.; Xiao, C.; Hu, D.; Wang, A.; Song, Y.; Ni, Y.; Jiang, G.; Duan, A. The Influence of Pore Structure and Acidity on the Hydrodesulfurization of Dibenzothiophene over NiMo-Supported Catalysts. *ACS Omega* **2020**, *5*, 15576–15585. [CrossRef] [PubMed]
77. Lecrenay, E.; Sakanishi, K.; Mochida, I. Catalytic hydrodesulfurization of gas oil and model sulfur compounds over commercial and laboratory-made CoMo and NiMo catalysts: Activity and reaction scheme. *Catal. Today* **1997**, *39*, 13–20. [CrossRef]
78. Pawelec, B.; Fierro, J.L.G.; Montesinos, A.; Zepeda, T.A. Influence of the acidity of nanostructured CoMo/P/Ti-HMS catalysts on the HDS of 4,6-DMDBT reaction pathways. *Appl. Catal. B Environ.* **2008**, *80*, 1–14. [CrossRef]
79. Wang, Y.; Yin, C.; Zhao, X.; Liu, C. Synthesis of bifunctional highly-loaded NiMoW catalysts and their catalytic performance of 4,6-DMDBT HDS. *Catal. Commun.* **2017**, *88*, 13–17. [CrossRef]